

- Patron NJ, Waller RF, Archibald JM, Keeling PJ. 2005. Complex protein targeting to dinoflagellate plastids. *J Mol Biol.* 348: 1015–1024.
- Patron NJ, Waller RF, Keeling PJ. 2006. A tertiary plastid uses genes from two endosymbionts. *J Mol Biol.* 357:1373–1382.
- Perkins FO. 1976. Zoospores of the oyster pathogen, *Dermocystidium marinum*. I. Fine structure of the conoid and other sporozoan-like organelles. *J Parasitol.* 62:959–974.
- Perkins FO. 1996. The structure of *Perkinsus marinus* (Mackin, Owen and Collier, 1950) Levine, 1978 with comments on taxonomy and phylogeny of *Perkinsus* spp. *J Shellfish Res.* 15:67–87.
- Perkins FO, Menzel RW. 1967. Ultrastructure of sporulation in the oyster pathogen *Dermocystidium marinum*. *J Invertebr Pathol.* 9:205–229.
- Richards TA, Dacks JB, Campbell SA, Blanchard JL, Foster PG, McLeod R, Roberts CW. 2006. Evolutionary origins of the eukaryotic shikimate pathway: gene fusions, horizontal gene transfer, and endosymbiotic replacements. *Eukaryot Cell.* 5:1517–1531.
- Rodríguez-Concepción M. 2004. The MEP pathway: a new target for the development of herbicides, antibiotics and antimalarial drugs. *Curr Pharm Des.* 10:2391–2400.
- Rodríguez-Ezpeleta N, Brinkmann H, Burey SC, Roure B, Burger G, Löffelhardt W, Bohnert HJ, Philippe H, Lang BF. 2005. Monophyly of primary photosynthetic eukaryotes: green plants, red algae, and glaucophytes. *Curr Biol.* 15:1325–1330.
- Rujan T, Martin W. 2001. How many genes in *Arabidopsis* come from cyanobacteria? An estimate from 386 protein phylogenies. *Trends Genet.* 17:113–120.
- Schott EJ, Vasta GR. 2003. The *PmSOD1* gene of the protistan parasite *Perkinsus marinus* complements the *sod2Δ* mutant of *Saccharomyces cerevisiae*, and directs an iron superoxide dismutase to mitochondria. *Mol Biochem Parasitol.* 126:81–92.
- Skovgaard A, Massana R, Balagué V, Saiz E. 2005. Phylogenetic position of the copepod-infesting parasite *Syndinium turbo* (Dinoflagellata, Syndinea). *Protist.* 156:413–423.
- Stelter K, El-Sayed NM, Seeber F. 2007. The expression of a plant-type ferredoxin redox system provides molecular evidence for a plastid in the early dinoflagellate *Perkinsus marinus*. *Protist.* 158:119–130.
- Sunila I, Hamilton RM, Dungan CF. 2001. Ultrastructural characteristics of the in vitro cell cycle of the protozoan pathogen of oysters, *Perkinsus marinus*. *J Eukaryot Microbiol.* 48:348–361.
- Teles-Grilo ML, Tato-Costa J, Duarte SM, Maia A, Casal G, Azevedo C. 2007. Is there a plastid in *Perkinsus atlanticus* (Phylum Perkinsozoa)? *Eur J Protistol.* 43:163–167.
- Thompson JD, Gibson TJ, Plewniak F, Jeanmougin F, Higgins DG. 1997. The CLUSTAL\_X windows interface: flexible strategies for multiple sequence alignment aided by quality analysis tools. *Nucleic Acids Res.* 25:4876–4882.
- van Dooren GG, Schwartzbach SD, Osafune T, McFadden GI. 2001. Translocation of proteins across the multiple membranes of complex plastids. *Biochim Biophys Acta.* 1541: 34–53.
- Villalba A, Reece KS, Ordás MC, Casas SM, Figueras A. 2004. Perkinsosis in molluscs: a review. *Aquat Living Resour.* 17:411–432.
- Whelan S, Goldman N. 2001. A general empirical model of protein evolution derived from multiple protein families using a maximum-likelihood approach. *Mol Biol Evol.* 18:691–699.
- Wilson RJM. 2005. Parasite plastids: approaching the endgame. *Biol Rev Camb Philos Soc.* 80:129–153.
- Wright AC, Ahmed H, Gauthier JD, Silva AM, Vasta GR. 2002. cDNA cloning and characterization of two iron superoxide dismutases from the oyster parasite *Perkinsus marinus*. *Mol Biochem Parasitol.* 123:73–77.
- Yoon HS, Hackett JD, Pinto G, Bhattacharya D. 2002. The single, ancient origin of chromist plastids. *Proc Natl Acad Sci USA.* 99:15507–15512.
- Yoon HS, Hackett JD, Van Dolah FM, Nosenko T, Lidie KL, Bhattacharya D. 2005. Tertiary endosymbiosis driven genome evolution in dinoflagellate algae. *Mol Biol Evol.* 22: 1299–1308.

Takashi Gojobori, Associate Editor

Accepted March 14, 2008

# Coinfection with Nonlethal Murine Malaria Parasites Suppresses Pathogenesis Caused by *Plasmodium berghei* NK65

Mamoru Niikura,<sup>1\*\*</sup> Shigeru Kamiya,<sup>†</sup> Kiyoshi Kita,<sup>‡</sup> and Fumie Kobayashi<sup>1†</sup>

Mixed infection with different *Plasmodium* species is often observed in endemic areas, and the infection with benign malaria parasites such as *Plasmodium vivax* or *P. malariae* has been considered to reduce the risk of developing severe pathogenesis caused by *P. falciparum*. However, it is still unknown how disease severity is reduced in hosts during coinfection. In the present study, we investigated the influence of coinfection with nonlethal parasites, *P. berghei* XAT (*Pb* XAT) or *P. yoelii* 17X (*Py* 17X), on the outcome of *P. berghei* NK65 (*Pb* NK65) lethal infection, which caused high levels of parasitemia and severe pathogenesis in mice. We found that the simultaneous infection with nonlethal *Pb* XAT or *Py* 17X suppressed high levels of parasitemia, liver injury, and body weight loss caused by *Pb* NK65 infection, induced high levels of reticulocytopenia, and subsequently prolonged survival of mice. In coinfecting mice, the immune response, including the expansion of B220<sup>int</sup>CD11c<sup>+</sup> cells and CD4<sup>+</sup> T cells and expression of IL-10 mRNA, was comparable to that in nonlethal infection. Moreover, the suppression of liver injury and body weight loss by coinfection was reduced in IL-10<sup>-/-</sup> mice, suggesting that IL-10 plays a role for a reduction of severity by coinfection with nonlethal malaria parasites. *The Journal of Immunology*, 2008, 180: 6877–6884.

Malaria is the infectious disease that causes incidence estimates of 2–3 million deaths and 300–500 million clinical cases in the world (1). There are four species of *Plasmodium* that infect humans: *Plasmodium falciparum*, *Plasmodium vivax*, *Plasmodium malariae*, and *Plasmodium ovale*. *P. falciparum* is the major human parasite responsible for high morbidity and mortality, and infection with *P. falciparum* is associated with developing fever, a high number of parasites in the blood, and pathogenesis, including severe anemia, body weight loss, and cerebral malaria in humans (2). The sensitive PCR-based techniques have revealed that coinfection with different *Plasmodium* species is common in developing countries (3, 4). In particular, the simultaneous presence of *P. vivax* or *P. malariae* during *P. falciparum* infection is often observed when the prevalence of *Plasmodium* infections in humans is analyzed in endemic areas (5–7) and it is known to reduce the risk of developing a high number of parasites in the blood as well as pathogenesis (8–11).

Murine malaria models have been used for understanding the induction of immune interaction in hosts and investigating factors associated with malarial defense mechanism. Coinfection with two different species and/or strains of murine malaria parasites has been shown to influence the parasitemia or mortality of each other (12). The development of experimental cerebral malaria caused by *Plasmodium berghei* (*Pb*)<sup>2</sup> ANKA was inhibited by the simulta-

neous presence of *Plasmodium yoelii yoelii* or *P. berghei* K173 (13, 14). However, it is still unknown how the disease severity is suppressed in simultaneous infection.

In the present study, we investigated the influence of simultaneous infection with nonlethal parasites, *P. berghei* XAT (*Pb* XAT) or *P. yoelii* 17X (*Py* 17X), on the outcome of *P. berghei* NK65 (*Pb* NK65) lethal infection, which causes high levels of parasitemia and pathogenesis such as body weight loss and liver injury in mice. First, we found that *Pb* XAT-immunized mice acquired resistance to *Pb* NK65 infection, although *Py* 17X-immunized mice were susceptible to *Pb* NK65 infection. By using these three species and strains, we examined how *Pb* XAT or *Py* 17X nonlethal infection modulated the immune responses such as cytokine production and cellular expansion during *Pb* NK65 lethal infection.

## Materials and Methods

### Mice

Female C57BL/6 (B6) mice were purchased from CLEA Japan and used at 5–6 wk of age. IL-10<sup>-/-</sup> mice on B6 background were purchased from The Jackson Laboratory. We used 20- to 24-wk-old female IL-10<sup>-/-</sup> mice (experiment 1), 5- to 6-wk-old male or female IL-10<sup>-/-</sup> mice (experiment 2), and age-matched female B6 mice in these studies. The genotype of female IL-10<sup>-/-</sup> mice used in experiments was verified by PCR. The experiments were approved by the Experimental Animal Ethics Committee at Kyorin University, and all experimental animals were kept on the specific pathogen-free unit at the animal facility with sterile bedding, food, and water.

### Parasites and infections

Malaria parasites were stored as frozen stocks in liquid nitrogen. *Pb* NK65 is a high-virulence strain and was originally obtained from Dr. M. Yoeli (New York University Medical Center, New York, NY). *Pb* XAT is a low-virulence derivative from *Pb* NK65 (15). A nonlethal isolate of *Py* 17X was originally obtained from Dr. J. Finnerty (National Institutes of Health, Bethesda, MD) and cloned by limiting dilution. Parasitized RBCs (pRBCs) of *Pb* NK65, *Pb* XAT, and *Py* 17X were generated in donor mice inoculated i.p. with each frozen stock of parasites. The donor mice were monitored for parasitemia daily and bled for experimental infection in ascending periods of parasitemia. Experimental mice were infected i.v. with  $1 \times 10^5$  pRBCs of a given parasite species or strain. Therefore, when mice were coinfecting with two species/strains of parasites, a total of  $2 \times 10^4$  pRBCs ( $1 \times 10^4$  of each parasite species/strain) were inoculated.

<sup>1</sup>Institute of Laboratory Animals, Graduate School of Medicine and <sup>2</sup>Department of Infectious Diseases, Faculty of Medicine, Kyorin University, Tokyo; and <sup>3</sup>Department of Biomedical Chemistry, Graduate School of Medicine, University of Tokyo, Tokyo, Japan

Received for publication July 12, 2007. Accepted for publication March 4, 2008.

The costs of publication of this article were defrayed in part by the payment of page charges. This article must therefore be hereby marked advertisement in accordance with 18 U.S.C. Section 1734 solely to indicate this fact.

<sup>1</sup>Address correspondence and reprint requests to Dr. Fumie Kobayashi and Dr. Mamoru Niikura, Faculty of Medicine, Kyorin University, 6-20-2 Shinkawa, Mitaka, Tokyo 181-8611, Japan. E-mail addresses: fumfum@ks.kyorin-u.ac.jp and mniikura@ks.kyorin-u.ac.jp

<sup>2</sup>Abbreviations used in this paper: *Pb*, *Plasmodium berghei*; *Py*, *Plasmodium yoelii*; pRBC, parasitized RBC; AST, aspartic aminotransferase; ALT, alanine aminotransferase.

Copyright © 2008 by The American Association of Immunologists, Inc. 0022-1767/08/\$20.00



Table I. Total spleen cell number in uninfected and infected mice ( $\times 10^6$ )<sup>a</sup>

	Days Postinfection			
	0	6	9	15
Uninfected	0.35 ± 0.17			
<i>Pb</i> NK65		1.05 ± 0.16	0.62 ± 0.25	
<i>Pb</i> XAT		0.74 ± 0.08	2.94 ± 0.75	4.41 ± 1.61
<i>Pb</i> NK65/ <i>Pb</i> XAT		0.74 ± 0.10	2.22 ± 0.70	6.52 ± 0.98
<i>Py</i> 17X		0.99 ± 0.18	4.63 ± 0.77	10.4 ± 3.02
<i>Pb</i> NK65/ <i>Py</i> 17X		1.28 ± 0.02	4.63 ± 1.34	11.6 ± 3.48

<sup>a</sup> Mice were infected with malarial parasites as described in the legend to Fig. 2. Spleens were obtained from uninfected and infected mice on days 6, 9, and 15 after infection. Results are expressed as means ± SD of three mice. Experiments were performed three times with similar results.

### Parasitemia

Parasitized RBCs were observed by microscopic examination of methanol-fixed tail blood smears stained for 45 min with 1% Giemsa diluted in phosphate buffer (pH 7.2). The number of pRBCs in 250 RBCs was enumerated when parasitemia exceeded 10%, whereas  $1 \times 10^4$  RBCs were examined when mice showed lower parasitemia. The percentage of parasitemia was calculated as follows: [(No. of pRBCs)/(Total no. of RBCs counted)]  $\times$  100.

### Measurement of body weights, hematocrits, and circulating reticulocytes

Body weights were measured by balance for animals (KN-661; Natume), and body weight loss was expressed as a percentage of the day 0 value. For hematocrit measurement, tail blood (50  $\mu$ l) was collected into a heparinized capillary tube and centrifuged at 13,000  $\times$  rpm for 5 min with a micro hematocrit centrifuge (HC-12A; Tomy). The hematocrit value was expressed as a percentage of the total blood volume. Reticulocytes in 250 RBCs were counted when reticulocytosis exceeded 20%, whereas  $1 \times 10^4$  RBCs were examined when mice showed lower reticulocytosis. The percentage of reticulocytosis was calculated as follows: [(No. of reticulocytes)/(Total no. of RBCs counted)]  $\times$  100.

### Histological examination and measurement of parameters of liver injury

Livers were obtained from infected mice on day 9 postinfection and fixed in 10% buffered formalin and embedded in paraffin. Six-micrometer-thick sections were stained with H&E. The blood was obtained from infected mice on day 9 and centrifuged at 500  $\times$  g for 10 min. The resulting supernatants were stored at  $-20^\circ\text{C}$  and used as plasma. The levels of aspartate aminotransferase (AST) and alanine aminotransferase (ALT) in plasma were determined at Nagahama Life Science Laboratory (Shiga, Japan).

### Flow cytometry

Flow cytometric analysis was performed on single-cell suspensions of spleen and peripheral blood cells as described previously (16). Total spleen cell numbers in uninfected and infected mice are shown in Table I. The following mAbs were used for analysis: FITC-conjugated anti-CD3 $\epsilon$  mAb (clone 145-2C11; eBioscience) and anti-CD4 mAb (clone RM4-5; eBioscience); PE-conjugated anti-CD11c mAb (clone N418; Miltenyi Biotec); allophycocyanin-conjugated anti-CD3 $\epsilon$  mAb (clone 145-2C11; eBioscience); and biotin-conjugated anti-CD45R mAb (B220; clone RA3-6B2; BD Pharmingen). MABs were added to cells in FACS buffer (1% BSA, 0.1% sodium azide in PBS) and incubated at 4°C for 30 min and the cells were washed with cold FACS buffer by centrifugation at 250  $\times$  g for 2 min. Biotinylated mAbs were followed by streptavidin-conjugated allophycocyanin (4°C, 30 min). After washing with FACS buffer, cells were fixed with 1% paraformaldehyde. Two-color flow cytometry was performed and analyzed with a FACSCalibur (BD Biosciences) using a FlowJo software (version 7.1.3, for Windows).

### Detection of cytokine mRNA in spleens

Spleens were removed from infected mice on day 9 postinfection and total RNA was isolated by Isogen (Nippon Gene) according to the manufacturer's protocol. The splenic RNA was reverse-transcribed by murine leukemia virus reverse transcriptase (Applied Biosystems) using random hexamer primers, and reverse transcriptase reaction was performed at 70°C for 10 min, at 25°C for 10 min, and at 42°C for 30 min. The reaction was

terminated by heating at 99°C for 5 min, and the cDNA products were stored at  $-20^\circ\text{C}$  until use. The 50  $\mu$ l PCR mixture contained 1  $\times$  TaKaRa Ex Taq buffer, 2.5 mM dNTP, 1  $\mu$ l cDNA products, 5 U/ $\mu$ l TaKaRa Ex Taq DNA polymerase, and 0.25  $\mu$ M of PCR primers. The primers used for PCR amplification were as follows: IL-10, 5'-GTG AAG ACT TTC TTT CAA ACA AAG, 3'-CTG CTC CAC TGC CTT GCT CTT ATT; IFN- $\gamma$ , 5'-TAC TGC CAC GGC ACA GTC ATT GAA, 3'-GCA GCG ACT CCT TTT CCG CTT CCT T;  $\beta$ -actin, 5'-CCA GCC TTC CTT CCT GGG TA, 3'-CTA GAA GCA TTT GCG GTG CA. Thirty cycles of PCR were performed on a thermal cycler (iCycler; Bio-Rad). Each cycle consisted of 30 s of denaturation at 94°C, 30 s of annealing at 60°C, and 1 min of extension at 72°C. The PCR products were analyzed on a 2% agarose gel stained with ethidium bromide.

### Cytokine assay

An ELISA for the detection of IFN- $\gamma$  or IL-10 in plasma was conducted as described previously (16). A rat anti-mouse IFN- $\gamma$  (clone R4-6A2; eBioscience) and a rat anti-mouse IL-10 (clone JES5-16E3; eBioscience) were used as the capture Abs, and a biotin-coupled rat anti-mouse IFN- $\gamma$  (clone XMG1.2; eBioscience) and IL-10 (clone JES5-2A5; eBioscience) were used as the detecting Abs. The concentration of cytokines in plasma was calculated from standard curves prepared with known quantities of murine recombinant IFN- $\gamma$  (Genzyme) and murine recombinant IL-10 (Pierce).

### Statistical analysis

For time-series comparisons, Student's *t* test and one- and two-way ANOVAs with Fisher's PLSD post hoc test were performed using Statcel program (OMS). Survival curves were compared using a log-rank test.  $p < 0.05$  was set as statistical significance of differences.

## Results

### Infection with *Pb* XAT but not *Pb* 17X induces protective immunity to *Pb* NK65

It has been shown that mice infected with *Pb* NK65 develop severe parasitemia and die within 2 wk, although mice infected with *Pb* XAT or *Py* 17X cure spontaneously around 3 wk of infection (15, 17). To examine whether primary infection with each of the two nonlethal parasites can induce protective immunity against *Pb* NK65 lethal infection, groups of C57BL/6 (B6) mice were infected with *Pb* XAT or *Py* 17X then challenged with *Pb* NK65 on day 30 after primary infection. As expected, mice cured from *Pb* XAT infection (*Pb* XAT-immunized mice) showed extremely low levels of parasitemia after secondary infection with *Pb* NK65 (Fig. 1A). On the contrary, mice cured from *Py* 17X infection (*Py* 17X-immunized mice) showed high levels of parasitemia, with some delay in onset of parasitemia, and eventually died after *Pb* NK65 infection (Fig. 1B). These results suggest that protective immunity to *Pb* NK65 is induced by immunizing mice with *Pb* XAT but not with heterologous *Py* 17X.



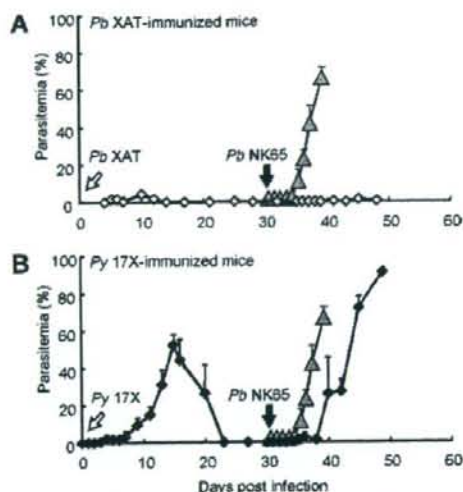


**FIGURE 1.** Immunization with *Pb* XAT but not *Py* 17X induces protective immunity to *Pbi* NK65. C57BL/6 mice were infected with  $1 \times 10^4$  pRBCs of *Pb* XAT (A) or *Py* 17X (B) (day 0, open arrows). On day 30 after primary infection (filled arrows), both groups of mice were challenged with  $1 \times 10^4$  pRBCs of *Pb* NK65. A, Course of parasitemia in immunized mice with *Pb* XAT ( $\diamond$ ). B, Course of parasitemia in immunized mice with *Py* 17X ( $\blacklozenge$ ). Course of parasitemia of unimmunized mice infected with *Pb* NK65 is inserted to figures (shaded triangles). Results are expressed as mean percentage parasitemia  $\pm$  SD of three mice. Experiments were performed three times with similar results.

*The pathogenesis during Pb NK65 infection is reduced by simultaneous infection with nonlethal malaria parasites*

To investigate whether the existence of nonlethal malaria parasite affects the outcome of *Pb* NK65 infection, B6 mice were infected with *Pb* NK65 and nonlethal parasites simultaneously. When mice were coinfecting with *Pb* NK65 and *Pb* XAT (*Pb* NK65/*Pb* XAT), they showed lower levels of parasitemia than did *Pb* NK65 singly

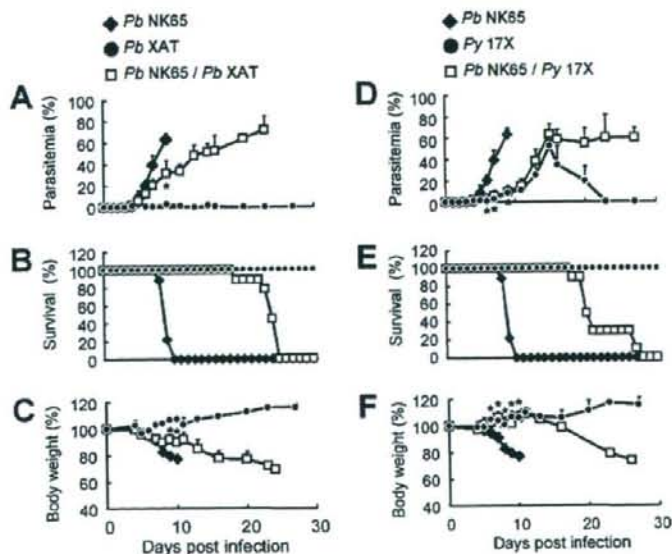
infected mice during early infection (Fig. 2A) and survived significantly longer than did *Pb* NK65 singly infected mice (Fig. 2B) ( $p = 0.0013$ ). Moreover, the body weight loss of the coinfecting mice was prevented early in infection (Fig. 2C) ( $p < 0.0005$  compared with *Pb* NK65-infected mice on days 9–10). Next, we examined the influence of coinfection with nonlethal *Py* 17X on the outcome of *Pb* NK65 infection. Although *Py* 17X immunization did not affect the outcome of *Pb* NK65 infection greatly (Fig. 1B), simultaneous infection with *Py* 17X (*Pb* NK65/*Py* 17X) suppressed severe parasitemia, mortality ( $p = 0.0005$ ), and the body weight loss ( $p < 0.0005$  on days 6–10) observed in *Pb* NK65 singly infected mice (Fig. 2, D–F).

*Coinfection with nonlethal malaria parasites induces reticulocytopenia*

To examine whether the existence of nonlethal malaria parasites affects the severe anemia caused by *Pb* NK65 infection, we determined the hematocrit in mice during *Pb* NK65 single infection and coinfection with *Pb* XAT or *Py* 17X. Coinfection with *Pb* XAT caused acute anemia as severe as did *Pb* NK65 single infection on day 9 postinfection, and the levels of hematocrit were also low on day 15 (Fig. 3A). Mice infected with *Pb* XAT did not cause acute severe anemia. In contrast, mice coinfecting with *Pb* NK65/*Py* 17X did not cause as severe anemia as for *Pb* NK65-infected mice on day 9, and their reducing pattern of hematocrit was similar to that in *Py* 17X singly infected mice (Fig. 3C).

Next, we determined the reticulocytopenia in infected mice. *Pb* NK65 singly infected mice did not show any reticulocytopenia during infection (Fig. 3B). Mice coinfecting with *Pb* NK65/*Pb* XAT showed the same levels of reticulocytopenia as did *Pb* XAT singly infected mice on day 9 postinfection. However, coinfecting mice showed much higher reticulocytopenia than that in *Pb* XAT singly infected mice from day 11 postinfection (Fig. 3B). As shown in Fig. 3D, reticulocytopenia in mice coinfecting with *Pb* NK65/*Py* 17X increased moderately, and their kinetics were similar to those in *Py* 17X singly infection. These results indicate that the severe anemia caused by *Pb* NK65 infection is suppressed by coinfection with *Py* 17X but not with *Pb* XAT. It is suggested that high levels of reticulocytopenia observed during *Pb* NK65/*Pb* XAT infection may

**FIGURE 2.** Coinfection of nonlethal *Pb* XAT or *Py* 17X suppresses the acute severe parasitemia and body weight loss caused by *Pb* NK65 infection in mice and prolonged their survival. C57BL/6 mice were inoculated with  $1 \times 10^4$  pRBCs of *Pb* NK65, *Pb* XAT, or *Py* 17X. When mice were coinfecting with two species/strains of parasites, a total of  $2 \times 10^4$  pRBCs were inoculated (*Pb* NK65/*Pb* XAT or *Pb* NK65/*Py* 17X). Results of coinfection are shown for *Pb* NK65/*Pb* XAT (A–C) or *Pb* NK65/*Py* 17X (D and E). A and D, Course of parasitemia. Asterisks indicate statistically significant differences ( $*, p < 0.001$  as compared with *Pb* NK65-infected mice). B and E, Survival rates. Differences between *Pb* NK65 singly infected mice and coinfecting mice are statistically significant ( $p < 0.001$ ). C and F, Body weights. Asterisks indicate statistically significant differences ( $*, p < 0.001$  as compared with *Pb* NK65-infected mice). Results are expressed as means  $\pm$  SD of five mice. Experiments were performed three times with similar results.



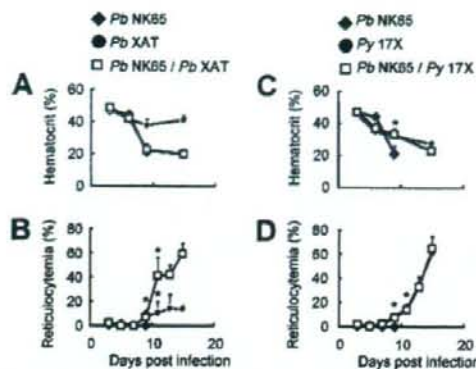


**FIGURE 3.** Coinfection with nonlethal malaria parasites induces reticulocytosis. Mice were infected with malarial parasites as described in the legend to Fig. 2. *A* and *C*, Blood (50  $\mu$ l) was collected from infected mice on days 3, 6, 9, and 15 after infection and hematocrit values were determined. *B* and *D*, Reticulocytosis was determined on days 3, 5, 7, 9, 11, 13, and 15 after infection. The percentage of reticulocytosis was calculated as follows: [(number of reticulocytes)/(total number of RBCs counted)]  $\times$  100. Asterisks indicate a statistically significant difference (\*,  $p < 0.001$  as compared with *Pb* NK65-infected mice). Results are expressed as means  $\pm$  SD of three mice. Experiments were performed three times with similar results.

be induced by severe anemia. The different outcome of the suppression of anemia and reticulocytosis between *Pb* NK65/*Pb* XAT- and *Pb* NK65/*Py* 17X-infected mice might be attributed to the difference in parasitemia during early infection.

#### Low levels of liver injury in mice coinfecting with nonlethal malaria parasites

To investigate whether the existence of nonlethal malaria parasites affects the liver injury caused by *Pb* NK65 infection, we performed histological examination of livers from mice during *Pb* NK65 single infection and coinfection with *Pb* XAT or *Py* 17X. As shown in Fig. 4, focal necrosis of the liver cells (Fig. 4, *B* and *F*, arrowheads) and dense infiltration of inflammatory cells such as mononuclear cells around the portal tracts (Fig. 4*F*, arrows) were observed in *Pb* NK65-infected mice. Mice coinfecting with *Pb* NK65/*Pb* XAT or *Pb* NK65/*Py* 17X also showed dense infiltration of inflammatory cells (Fig. 4, *G* and *H*, arrows), but focal necroses were not observed in the liver (Fig. 4, *C* and *D*).

We determined the levels of AST and ALT, which are parameters of liver injury, in the plasma. *Pb* NK65-infected mice, in which the focal necroses of liver cells were observed, showed the significantly high concentration of AST and ALT compared with uninfected control mice (Fig. 4, *I* and *J*). The levels of AST and ALT in coinfecting mice were quite low and almost the same as those in *Pb* XAT or *Py* 17X singly infected mice.

#### Coinfection with nonlethal parasites accelerates *B220*<sup>+</sup>*CD11c*<sup>+</sup> cell expansion in spleen and peripheral blood

To examine the expansion of the *CD11c*<sup>+</sup> cell populations during malaria, additional experiments were performed using peripheral blood and spleen obtained from infected mice by flow cytometry in each time point after infection. It was notable that the *B220*<sup>+</sup>*CD11c*<sup>+</sup> cell population significantly increased in peripheral blood from *Pb* NK65/*Pb* XAT- or *Pb* NK65/*Py* 17X-coinfecting mice on day 6 postinfection (Fig. 5*A*, upper panels). Their expansion was comparable to that observed in *Pb* XAT or *Py* 17X

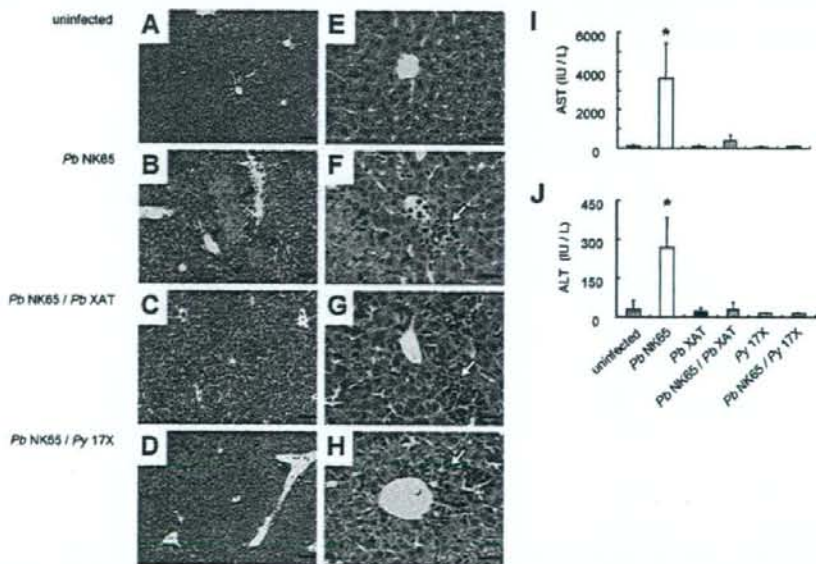


**FIGURE 4.** The existence of nonlethal malaria parasites prevents the liver injury caused by *Pb* NK65 infection. Mice were infected with malarial parasites as described in the legend to Fig. 2. Livers and plasma were obtained from infected mice on day 9 after infection and from uninfected mice. *A-H*, Histological analysis was performed after staining with H&E. Typical results of uninfected mice (*A* and *E*), mice singly infected with *Pb* NK65 (*B* and *F*), and mice coinfecting with *Pb* NK65/*Pb* XAT (*C* and *G*) or *Pb* NK65/*Py* 17X (*D* and *H*) are shown. *A-D*, The scale bar indicates 100  $\mu$ m. Arrowheads indicate focal necrosis of the liver cells. *E-H*, The scale bar indicates 40  $\mu$ m. Arrows indicate dense infiltration of inflammatory cells. *I* and *J*, Levels of AST and ALT. Asterisks indicate a statistically significant difference (\*,  $p < 0.001$  as compared with uninfected control mice). Results are expressed as means  $\pm$  SD of three mice. Experiments were performed three times with similar results and the representative data are shown.



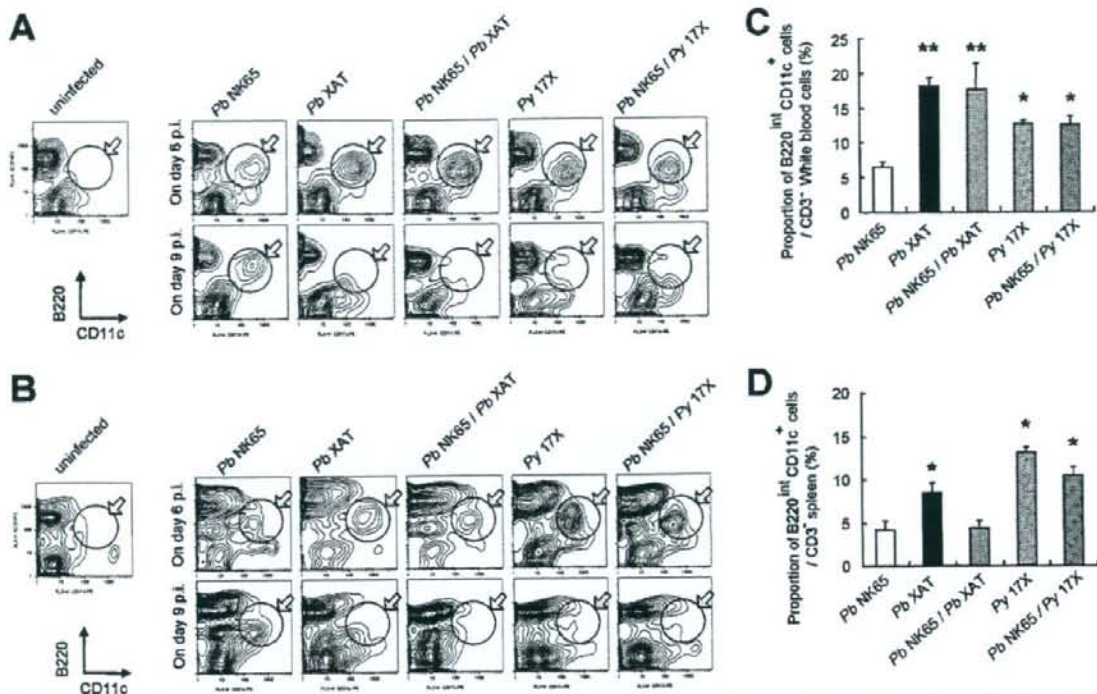


**FIGURE 5.** Coinfection with nonlethal parasites accelerates B220<sup>int</sup>CD11c<sup>+</sup> cell expansion in spleen and peripheral blood. Peripheral blood and spleen were obtained from infected mice as described in the legend to Fig. 2 on days 6 and 9 after infection and from uninfected mice. Analyses of CD11c<sup>+</sup> cell population in peripheral blood (A and C) and spleen (B and D) from infected mice were performed by flow cytometry. Expression of B220 and CD11c was analyzed in the gate of CD3<sup>+</sup>. A and B, Contour plots of B220<sup>int</sup>CD11c<sup>+</sup> cell population (day 6, upper panels; day 9, lower panels). p.i., Post infection. Experiments were performed three times with similar results and the representative results are shown. C and D, The proportion of B220<sup>int</sup>CD11c<sup>+</sup> cells in CD3<sup>+</sup> cells is shown (on day 6 postinfection). Asterisks indicate a statistically significant difference (\*,  $p < 0.005$ ; \*\*,  $p < 0.001$  as compared with *Pb* NK65-infected mice). Results are expressed as means  $\pm$  SD of three mice.

single infection, respectively (Fig. 5C). The B220<sup>int</sup>CD11c<sup>+</sup> cell population in those four groups of mice decreased on day 9 postinfection (Fig. 5A, lower panels). Although B220<sup>int</sup>CD11c<sup>+</sup> cells in *Pb* NK65-infected mice also expanded on day 6 postinfection, they were much less than those in coinfecting or nonlethal parasite-infected mice. The cell population in *Pb* NK65-infected mice further expanded on day 9 postinfection, when no other groups of mice showed the expansion (Fig. 5A). The B220<sup>int</sup>CD11c<sup>+</sup> cell population of spleen showed a similar pattern to that of peripheral blood (Fig. 5B), but the proportion of the cells in *Pb* NK65/*Pb* XAT-infected mice was lower than that in *Pb* XAT-infected mice on day 6 postinfection (Fig. 5D). These results suggested that coinfection with nonlethal parasites accelerated much more B220<sup>int</sup>CD11c<sup>+</sup> cell expansion than did *Pb* NK65 single infection during the early phase of infection.

#### Coinfection with nonlethal parasites induces CD4<sup>+</sup> T cell expansion in spleen

We analyzed the kinetics of CD4<sup>+</sup> T cell expansion in spleen during single and mixed infection (Fig. 6). Significant expansion of splenic CD4<sup>+</sup> T cells in *Pb* XAT- or *Py* 17X-infected mice was observed from day 9 postinfection. In contrast, *Pb* NK65-infected mice did not show the increased levels of CD4<sup>+</sup> T cells even on day 9 postinfection. Mice coinfecting with *Pb* NK65/*Pb* XAT or *Pb* NK65/*Py* 17X had almost the same number of splenic CD4<sup>+</sup> T cells as did *Pb* XAT- or *Py* 17X-infected mice, respectively.

#### Enhanced levels of IL-10 mRNA during coinfection and nonlethal infection

IFN- $\gamma$  and IL-10 have been shown to be associated with protection and exacerbation during *P. berghei* and *P. yoelii* malaria (17, 18).

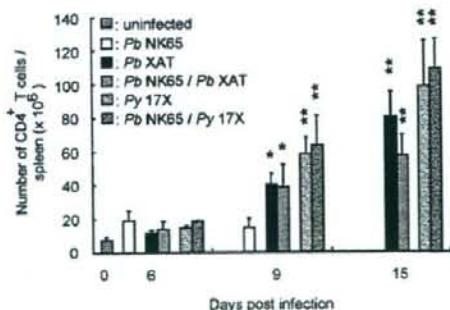


**FIGURE 6.** Coinfection with nonlethal parasites induces CD4<sup>+</sup> T cell expansion in spleen. Spleens were obtained from infected mice as described in the legend to Fig. 2 on days 6, 9, and 15 after infection and from uninfected mice. Splenic CD3<sup>+</sup>CD4<sup>+</sup> cells were analyzed by flow cytometry and total numbers of CD4<sup>+</sup> T cells in spleen were calculated. Asterisks indicate a statistically significant difference (\*,  $p < 0.05$ ; \*\*,  $p < 0.005$  as compared with uninfected control mice). Results are expressed as means  $\pm$  SD of three mice. Experiments were performed three times with similar results.



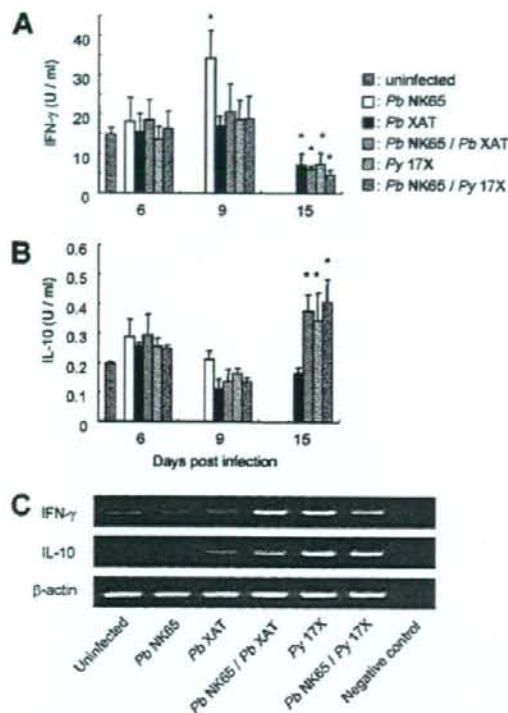


**FIGURE 7.** Enhanced levels of IL-10 mRNA during coinfection and nonlethal infection. **A** and **B**, Levels of IFN- $\gamma$  or IL-10 were determined by ELISA. Plasma was collected from uninfected mice and infected mice on days 6, 9, and 15 post infection. **A**, Levels of IFN- $\gamma$  in plasma. **B**, Levels of IL-10 in plasma. Asterisks indicate a statistically significant difference as compared with uninfected mice ( $p < 0.001$ ). **C**, Total RNA was isolated from spleen of uninfected and infected mice as described in the legend to Fig. 2 on day 9 and subjected to RT-PCR using cytokine-specific primers. The samples without RNA template were used as negative control. Note that coinfecting mice (*Pb NK65/Pb XAT*, *Pb NK65/Py 17X*) show IL-10 mRNA expression that is comparable to nonlethal parasite-infected mice (*Pb XAT*, *Py 17X*). Experiments were performed three times with similar results.

To examine whether these cytokines are associated with the suppression of *Pb NK65*-caused pathogenesis by coinfection with the nonlethal malaria parasites, we determined the levels of cytokines in plasma and cytokine mRNA in spleens from singly infected or coinfecting mice (Fig. 7). *Pb NK65* singly infected mice showed a high level of IFN- $\gamma$  in plasma on day 9 compared with that in uninfected mice (Fig. 7A). Although the plasma IFN- $\gamma$  levels in coinfecting mice or nonlethal singly infected mice on days 6 and 9 were not different from those in uninfected mice, these mice showed significantly lower levels of IFN- $\gamma$  than did uninfected mice on day 15. In contrast, strong IFN- $\gamma$  mRNA expression was detected in the spleen from mice singly infected with *Py 17X* and coinfecting with *Pb NK65/Pb XAT* and *Pb NK65/Py 17X*, compared with that observed in uninfected mice on day 9 (Fig. 7C). However, *Pb NK65* singly infected mice did not show high levels of IFN- $\gamma$  mRNA expression. These results suggested that spleen might not be a main organ for production of IFN- $\gamma$ , which was involved in severe pathogenesis during *Pb NK65* single infection (18), but the association of IFN- $\gamma$  with suppressive pathogenesis by coinfection was still unclear.

The levels of IL-10 in plasma from single or coinfecting mice on days 6 and 9 were not different from uninfected mice, but coinfecting

mice as well as nonlethal *Py 17X* singly infected mice showed elevated levels of IL-10 on day 15 (Fig. 7B). Although *Pb NK65* singly infected mice showed only faint expression of IL-10 mRNA on day 9, mice coinfecting with *Pb NK65/Pb XAT* or *Pb NK65/Py 17X* showed strong IL-10 mRNA expression, which was comparable to that observed in mice during *Pb XAT* or *Py 17X* single infection (Fig. 7C). IL-10 mRNA was not detected in spleen from uninfected mice. These results led us to hypothesize that the enhanced levels of IL-10 may be involved in suppression of pathogenesis during coinfection.

#### *IL-10-deficient mice fail to receive benefits by coinfection with nonlethal malaria parasites*

To examine whether IL-10 is associated with the suppression of the pathogenesis caused by coinfection, we determined the parasitemia, mortality, and the body weight of *Pb NK65*-infected IL-10<sup>-/-</sup> mice coinfecting with *Pb XAT* or *Py 17X*. *Pb NK65/Pb XAT*-coinfecting wild-type mice survived by day 21 (Fig. 8D), confirming the data obtained in Fig. 2B. In contrast, IL-10<sup>-/-</sup> mice coinfecting with *Pb NK65/Pb XAT* began to die from day 10, and all mice died by day 21 postinfection (Fig. 8D) ( $p = 0.034$ ). Moreover, their body weights were significantly lower than coinfecting wild-type mice (Fig. 8E) ( $p < 0.001$  on days 9, 11, and 13), although their parasitemia did not increase from day 11 (Fig. 8F). Similarly, *Pb NK65/Py 17X*-coinfecting IL-10<sup>-/-</sup> mice began to die earlier than did wild-type mice (Fig. 8G), and their body weights were also lower than those of wild-type mice (Fig. 8H) ( $p < 0.001$  on days 9, 13, and 18). During the period when coinfecting IL-10<sup>-/-</sup> mice began to die, they developed liver injury (Fig. 8, M and O), which was not observed in coinfecting wild-type mice (Fig. 8, L and N). In contrast, the parasitemia, mortality, the body weight, and development of liver injury of *Pb NK65* singly infected IL-10<sup>-/-</sup> mice were not different from those of wild-type mice (Fig. 8, A-C, J, and K). Altogether, these results suggest that IL-10 may be involved in the suppressive effect of coinfection with nonlethal malaria parasites on the outcome of lethal *Pb NK65* infection.

#### Discussion

In the present study, we investigated the influence of simultaneous infection with nonlethal murine malaria parasites, *Pb XAT* or *Py 17X*, on the outcome of the lethal *Pb NK65* infection. *Pb NK65* infection caused acute high parasitemia and pathogenesis, including body weight loss, severe anemia, and liver injury in mice. We found herein that the coinfection with nonlethal *Pb XAT* or *Py 17X* reduced such pathogenesis caused by *Pb NK65* infection and prolonged survival of mice (Figs. 2-4). Because low levels of parasitemia and body weight loss in coinfecting mice were observed from day 6 to 7 (Fig. 2), we postulated that T/B cell-mediated immunity would be involved in the suppressive effects of simultaneous infection with nonlethal parasites on lethal *Pb NK65* infection and examined the response of dendritic cells and CD4<sup>+</sup> T cells.

The large expansion of B220<sup>int</sup>CD11c<sup>+</sup> cells was observed in spleen and peripheral blood from coinfecting mice on day 6, which was comparable to that from nonlethal parasite-infected mice (Fig. 5). These results suggest that expansion of B220<sup>int</sup>CD11c<sup>+</sup> cells in coinfecting mice may be accelerated by nonlethal parasite relative to lethal parasite infection. It has been reported that CD11c<sup>+</sup> dendritic cells are one of the professional APCs. As the murine plasmacytoid dendritic cell subset has been shown to coexpress CD11c and B220 (19-20), one would speculate that B220<sup>int</sup>CD11c<sup>+</sup> cells expanded during nonlethal infection or coinfection might be one of the murine plasmacytoid dendritic cell subpopulations. Further characterization of the B220<sup>int</sup>CD11c<sup>+</sup> cells, however, is needed for identification of these cells. In *Pb NK65*-infected mice, the peak expansion of B220<sup>int</sup>CD11c<sup>+</sup> cells was observed on day 9, when these cells



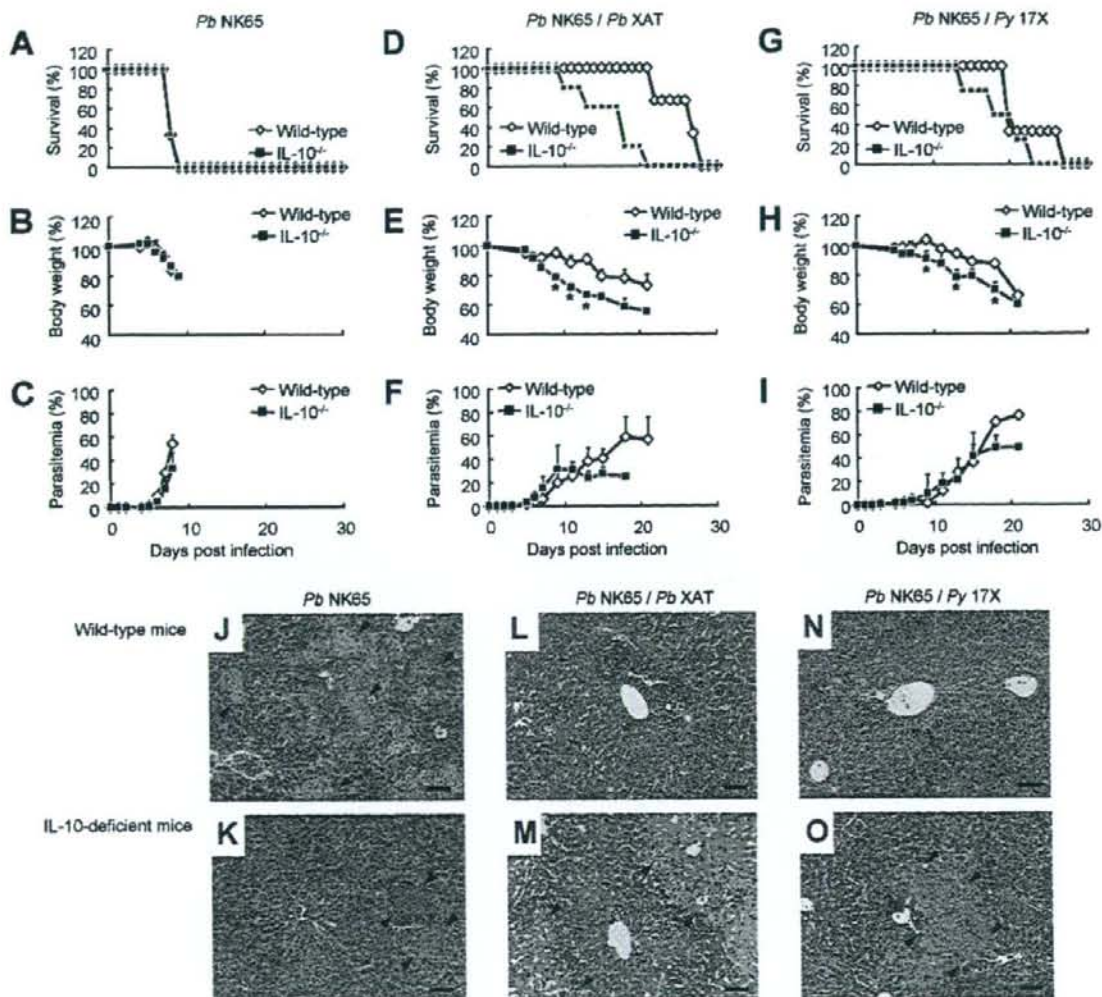


**FIGURE 8.** IL-10-deficient mice fail to receive benefits by coinfection with nonlethal malaria parasites. IL-10<sup>-/-</sup> mice and age-matched wild-type mice were singly infected with *Pb* NK65, coinfecting with *Pb* NK65/*Pb* XAT, or coinfecting with *Pb* NK65/*Py* 17X. Survival rates (A, D, and G), body weight (B, E and H), and course of parasitemia (C, F, and I) are shown. Asterisks indicate a statistically significant difference (\*,  $p < 0.001$  as compared with wild-type mice). Results are expressed as means  $\pm$  SD of three to five mice. Histological analysis of liver was performed after staining with H&E (J–O). Livers were obtained from infected wild-type mice (J, L, and N) and IL-10<sup>-/-</sup> mice (K, M, and O) immediately after death from day 10 to 22 after infection. The scale bar indicates 100  $\mu$ m. Arrowheads indicate focal necrosis of the liver cells. Experiments were performed twice with similar results and the representative data are shown.

began to decrease in coinfecting mice as well as nonlethal *Pb* XAT- or *Py* 17X-infected mice. Because *Pb* NK65 parasites multiply quickly, especially in early phase of infection, earlier expansion of B220<sup>int</sup>CD11c<sup>+</sup> cells may be the key for the suppression of pathogenesis during coinfection.

In contrast, mice coinfecting with *Pb* NK65 and nonlethal *Pb* XAT or *Py* 17X showed increased levels of CD4<sup>+</sup> T cells from day 9 that were comparable to nonlethal parasite-infected mice (Fig. 6). Dendritic cells have been shown to activate naive T cells and play a crucial role in the initiation of immune responses (21–23). It is possible that the expansion of splenic CD4<sup>+</sup> T cells might be induced by B220<sup>int</sup>CD11c<sup>+</sup> cells that had been expanded earlier (on day 6), and then the expanded CD4<sup>+</sup> T cells might be involved in suppression of pathogenesis in coinfecting mice. CD4<sup>+</sup> T cells have been shown to

play both protective and pathological roles during malaria infection (24–25). However, it seems that CD4<sup>+</sup> T cells would play protective roles during coinfection with lethal and nonlethal malaria parasites.

IL-10, which is produced by Th2 cells in CD4<sup>+</sup> T cell categories, inhibits inflammatory cytokines such as IFN- $\gamma$ , TNF- $\alpha$  (26), and IL-12 (27). In malaria, IL-10 as well as TGF- $\beta$  has been shown to be critical for host survival during *P. berghei* ANKA (28, 29) and *P. chabaudi* AS (30) infection. In the present study, *Pb* NK65/*Pb* XAT- or *Pb* NK65/*Py* 17X-coinfecting mice showed high levels of IL-10 mRNA comparable to those in nonlethal *Pb* XAT- or *Py* 17X-infected mice (Fig. 7C), although *Pb* NK65-infected mice showed only a faint level of IL-10 mRNA. Moreover, high levels of IL-10 in plasma were followed by the IL-10 mRNA expression in coinfecting mice on day 15 when IFN- $\gamma$  production was



suppressed (Fig. 7). These results suggest that IL-10 may be involved in the suppression of pathogenesis in coinfecting mice.

As expected, the suppressive effect of coinfection with nonlethal *Pb* XAT or *Py* 17X on severe body weight loss, liver injury, and mortality during *Pb* NK65 infection was reduced in IL-10<sup>-/-</sup> mice (Fig. 8), suggesting that IL-10 was involved in suppression of exacerbation of infection in simultaneous infection. The excessive inflammation has been shown to be able to account for body weight loss, liver injury, and mortality in mice infected with *Pb* NK65 (18, 31). Therefore, it is probable that enhancement of IL-10 would have suppressed the excessive inflammation caused by *Pb* NK65 and subsequently led to suppression of pathogenesis. In contrast, mortality as well as body weight loss in IL-10<sup>-/-</sup> mice during coinfection were not identical with those in *Pb* NK65 singly infected IL-10<sup>-/-</sup> mice, suggesting that other regulatory factors, such as TGF- $\beta$  (30), may be involved in suppression of pathogenesis.

In the late phase of infection, IL-10<sup>-/-</sup> mice coinfecting with *Pb* NK65/*Pb* XAT or *Pb* NK65/*Py* 17X had lower levels of parasitemia than that in wild-type mice. These results suggest that although IL-10 plays an important role for suppression of liver injury, it may be also involved in suppression of clearance of malaria parasites and cause death by severe anemia in the late phase of coinfection. It has been shown that during *Py* 17XL lethal infection, IL-10 is involved in the exacerbation of infection because depletion of IL-10 prolonged survival of hosts and made some mice resolve the infection (17, 32, 33). IL-10 might have dual roles, protective and pathological, in mice coinfecting with lethal and nonlethal malaria parasites.

Our findings showing the beneficial influence of coinfection with nonlethal *Pb* XAT or *Py* 17X to hosts during *Pb* NK65 infection indicate that suppression of disease severity induced by coinfection occurs in not only cerebral malaria but also pathogenesis such as body weight loss and liver injury. Our data suggest that the beneficial influence of coinfection with nonlethal malaria parasites may not be species-specific because a different species of malaria parasites, *Py* 17X, also induced protective immunity to *Pb* NK65 lethal infection by simultaneous infection (Fig. 2). In endemic areas, coinfections have made diagnosis and treatment difficult because host immune responses induced by each of the different *Plasmodium* spp. are mutually interfered with in a complicated manner. Results obtained from *in vivo* models of coinfection with murine malaria parasites would contribute to understand the host immune responses during mixed infection with different *Plasmodium* spp.

## Disclosures

The authors have no financial conflicts of interest.

## References

- Snow, R. W., M. H. Craig, U. Deichmann, and D. le Sueur. 1999. A preliminary continental risk map for malaria mortality among African children. *Parasitol. Today* 15: 99–104.
- Breman, J. G. 2001. The ears of the hippopotamus: manifestations, determinants, and estimates of the malaria burden. *Am. J. Trop. Med. Hyg.* 64: 1–11.
- Siribal, S., S. Nakasin, S. Loareesuwan, and P. Chavalitshewinkoon-Petmitr. 2004. Identification of human malaria parasites and detection of mixed infection in Thai patients by nested PCR. *Southeast Asian J. Trop. Med. Public Health* 35: 5–9.
- Imwong, M., S. Pokrityayakamee, A. C. Griner, L. Rénia, F. Letourneur, S. Loareesuwan, N. J. White, and G. Snounou. 2005. Practical PCR genotyping protocols for *Plasmodium vivax* using *Pvcs* and *Pvmp1*. *Malar. J.* 4: 20.
- Mehlota, R. K., K. Lorry, W. Kastens, S. M. Miller, M. P. Alpers, M. Bockarie, J. W. Kazura, and P. A. Zimmerman. 2000. Random distribution of mixed species malaria infections in Papua New Guinea. *Am. J. Trop. Med. Hyg.* 62: 225–231.
- Pinto, J., C. A. Sousa, V. Gil, L. Gonçalves, D. Lopes, V. E. do Rosário, and J. D. Charlot. 2000. Mixed-species malaria infections in the human population of São Tomé island, west Africa. *Trans. R. Soc. Trop. Med. Hyg.* 94: 256–257.
- Ebrahimzadeh, A., B. Fouladi, and A. Fazaeli. 2007. High rate of detection of mixed infections of *Plasmodium vivax* and *Plasmodium falciparum* in south-east of Iran, using nested PCR. *Parasitol. Int.* 56: 61–64.
- Mason, D. P., F. E. McKenzie, and W. H. Bossert. 1999. The blood-stage dynamics of mixed *Plasmodium malariae*-*Plasmodium falciparum* infections. *J. Theor. Biol.* 198: 549–566.
- Mason, D. P., and F. E. McKenzie. 1999. Blood-stage dynamics and clinical implications of mixed *Plasmodium vivax*-*Plasmodium falciparum* infections. *Am. J. Trop. Med. Hyg.* 61: 367–374.
- McQueen, P. G., and F. E. McKenzie. 2006. Competition for red blood cells can enhance *Plasmodium vivax* parasitemia in mixed-species malaria infections. *Am. J. Trop. Med. Hyg.* 75: 112–125.
- Luxemburger, C., F. Ricci, F. Nosten, D. Raimond, S. Bathet, and N. J. White. 1997. The epidemiology of severe malaria in an area of low transmission in Thailand. *Trans. R. Soc. Trop. Med. Hyg.* 91: 256–262.
- Snounou, G., T. Bourne, W. Jarra, S. Vitiyakosol, J. C. Wood, and K. N. Brown. 1992. Assessment of parasite population dynamics in mixed infections of rodent plasmodia. *Parasitology* 105: 363–374.
- Voza, T., A. M. Vignario, E. Beloune, A. C. Gruner, J. C. Deschemin, M. Kayibanda, F. Delmas, C. J. Janse, B. Franke-Payard, A. P. Waters, et al. 2005. Species-specific inhibition of cerebral malaria in mice coinfecting with *Plasmodium* spp. *Infect. Immun.* 73: 4777–4786.
- Mitchell, A. J., A. M. Hansen, L. Hee, H. J. Ball, S. M. Potter, J. C. Walker, and N. H. Hunt. 2005. Early cytokine production is associated with protection from murine cerebral malaria. *Infect. Immun.* 73: 5645–5653.
- Waki, S., J. Tamura, M. Imanaka, S. Ishikawa, and M. Suzuki. 1982. *Plasmodium berghei*: isolation and maintenance of an irradiation attenuated strain in the nude mouse. *Exp. Parasitol.* 53: 335–340.
- Kobayashi, F., M. Niikura, S. Waki, T. Matsui, T. Fujino, T. Tsuruhara, and S. Kamiya. 2007. *Plasmodium berghei* XAT: contribution of  $\gamma\delta$  T cells to host defense against infection with blood-stage nonlethal malaria parasite. *Exp. Parasitol.* 117: 368–375.
- Kobayashi, F., T. Morii, T. Matsui, T. Fujino, Y. Watanabe, W. P. Weidanz, and M. Tsuji. 1996. Production of IL-10 during malaria caused by lethal and nonlethal variants of *Plasmodium yoelii yoelii*. *Parasitol. Res.* 82: 385–391.
- Waki, S., S. Uehara, K. Kanbe, K. Ono, M. Suzuki, and H. Nariuchi. 1992. The role of T cells in pathogenesis and protective immunity to murine malaria. *Immunology* 75: 646–651.
- Nakano, H., M. Yanagita, and M. D. Gunn. 2001. CD11c<sup>+</sup>B220<sup>+</sup>Gr-1<sup>+</sup> cells in mouse lymph nodes and spleen display characteristics of plasmacytoid dendritic cells. *J. Exp. Med.* 194: 1171–1178.
- Björck, P. 2001. Isolation and characterization of plasmacytoid dendritic cells from Flt3 ligand and granulocyte-macrophage colony-stimulating factor-treated mice. *Blood* 98: 3520–3526.
- Inaba, K., and R. M. Steinman. 1984. Resting and sensitized T lymphocytes exhibit distinct stimulatory (antigen-presenting cell) requirements for growth and lymphokine release. *J. Exp. Med.* 160: 1717–1735.
- Knight, S. C., and A. J. Stagg. 1993. Antigen-presenting cell types. *Curr. Opin. Immunol.* 5: 374–382.
- Metlay, J. P., M. D. Witmer-Pack, R. Agger, M. T. Crowley, D. Lawless, and R. M. Steinman. 1990. The distinct leukocyte integrins of mouse spleen dendritic cells as identified with new hamster monoclonal antibodies. *J. Exp. Med.* 171: 1753–1771.
- Yoneto, T., T. Yoshimoto, C. R. Wang, Y. Takahama, M. Tsuji, S. Waki, and H. Nariuchi. 1999. Gamma interferon production is critical for protective immunity to infection with blood-stage *Plasmodium berghei* XAT but neither NO production nor NK cell activation is critical. *Infect. Immun.* 67: 2349–2356.
- Langhorne, J., S. J. Meding, K. Eichmann, and S. S. Cillard. 1989. The response of CD4<sup>+</sup> T cells to *Plasmodium chabaudi chabaudi*. *Immunol. Rev.* 112: 71–94.
- Mosmann, T. R., and K. W. Moore. 1991. The role of IL-10 in crossregulation of TH1 and TH2 responses. *Immunol. Today* 12: A49–A53.
- Xu, X., K. Sumita, C. Feng, X. Xiong, H. Shen, S. Maruyama, M. Kanoh, and Y. Asano. 2001. Down-regulation of IL-12 p40 gene in *Plasmodium berghei*-infected mice. *J. Immunol.* 167: 235–241.
- Tan, R. S., A. U. Kara, C. Feng, Y. Asano, and R. Sinniah. 2000. Differential IL-10 expression in interferon regulatory factor-1 deficient mice during *Plasmodium berghei* blood-stage infection. *Parasite Immunol.* 22: 425–435.
- Kossodo, S., C. Monso, P. Juillard, T. Velu, M. Goldman, and G. E. Grau. 1997. Interleukin-10 modulates susceptibility in experimental cerebral malaria. *Immunology* 91: 536–540.
- Li, C., L. A. Sanni, F. Omer, E. Riley, and J. Langhorne. 2003. Pathology of *Plasmodium chabaudi chabaudi* infection and mortality in IL-10-deficient mice are ameliorated by anti-tumor necrosis factor  $\alpha$  and exacerbated by anti-transforming growth factor  $\beta$  antibodies. *Infect. Immun.* 71: 4850–4856.
- Yoshimoto, T., Y. Takahama, C. R. Wang, T. Yoneto, S. Waki, and H. Nariuchi. 1998. A pathogenic role of IL-12 in blood-stage murine malaria lethal strain *Plasmodium berghei* NK65 infection. *J. Immunol.* 160: 5500–5505.
- Omer, F. M., J. B. de Souza, and E. M. Riley. 2003. Differential induction of TGF- $\beta$  regulates proinflammatory cytokine production and determines the outcome of lethal and nonlethal *Plasmodium yoelii* infections. *J. Immunol.* 171: 5430–5436.
- Kobayashi, F., H. Ishida, T. Matsui, and M. Tsuji. 2000. Effects of *in vivo* administration of anti-IL-10 or anti-IFN- $\gamma$  monoclonal antibody on the host defense mechanism against *Plasmodium yoelii yoelii* infection. *J. Vet. Med. Sci.* 6: 583–587.



## Structures of *Trypanosoma cruzi* Dihydroorotate Dehydrogenase Complexed with Substrates and Products: Atomic Resolution Insights into Mechanisms of Dihydroorotate Oxidation and Fumarate Reduction<sup>†,‡</sup>

Daniel Ken Inaoka,<sup>§,||</sup> Kimitoshi Sakamoto,<sup>§</sup> Hironari Shimizu,<sup>§</sup> Tomoo Shiba,<sup>‡</sup> Genji Kurisu,<sup>‡</sup> Takeshi Nara,<sup>#</sup> Takashi Aoki,<sup>#</sup> Kiyoshi Kita,<sup>\*,§</sup> and Shigeharu Harada<sup>\*,○</sup>

Department of Biomedical Chemistry, Graduate School of Medicine, The University of Tokyo, Tokyo 113-0033, Japan, Department of Life Sciences, Graduate School of Arts and Sciences, The University of Tokyo, Tokyo 153-8902, Japan, Department of Molecular and Cellular Parasitology, Juntendo University, Tokyo 113-8421, Japan, and Department of Applied Biology, Graduate School of Science and Technology, Kyoto Institute of Technology, Kyoto 606-8585, Japan

Received March 11, 2008; Revised Manuscript Received July 25, 2008

**ABSTRACT:** Dihydroorotate dehydrogenase (DHOD) from *Trypanosoma cruzi* (TcDHOD) is a member of family 1A DHOD that catalyzes the oxidation of dihydroorotate to orotate (first half-reaction) and then the reduction of fumarate to succinate (second half-reaction) in the *de novo* pyrimidine biosynthesis pathway. The oxidation of dihydroorotate is coupled with the reduction of FMN, and the reduced FMN converts fumarate to succinate in the second half-reaction. TcDHOD are known to be essential for survival and growth of *T. cruzi* and a validated drug target. The first-half reaction mechanism of the family 1A DHOD from *Lactococcus lactis* has been extensively investigated on the basis of kinetic isotope effects, mutagenesis and X-ray structures determined for ligand-free form and in complex with orotate, the product of the first half-reaction. In this report, we present crystal structures of TcDHOD in the ligand-free form and in complexes with an inhibitor, physiological substrates and products of the first and second half-reactions. These ligands bind to the same active site of TcDHOD, which is consistent with the one-site ping-pong Bi-Bi mechanism demonstrated by kinetic studies for family 1A DHODs. The binding of ligands to TcDHOD does not cause any significant structural changes to TcDHOD, and both reduced and oxidized FMN cofactors are in planar conformation, which indicates that the reduction of the FMN cofactor with dihydroorotate produces anionic reduced FMN. Therefore, they should be good models for the enzymatic reaction pathway of TcDHOD, although orotate and fumarate bind to TcDHOD with the oxidized FMN and dihydroorotate with the reduced FMN in the structures determined here. Cys130, which was identified as the active site base for family 1A DHOD (Fagan, R. L., Jensen, K. F., Bjornberg, O., and Palfey, B. A. (2007) *Biochemistry* 46, 4028–4036.), is well located for abstracting a proton from dihydroorotate C5 and transferring it to outside water molecules. The bound fumarate is in a twisted conformation, which induces partial charge separation represented as C<sub>2</sub><sup>δ-</sup> and C<sub>3</sub><sup>δ+</sup>. Because of this partial charge separation, the thermodynamically favorable reduction of fumarate with reduced FMN seems to proceed in the way that C<sub>2</sub><sup>δ-</sup> accepts a proton from Cys130 and C<sub>3</sub><sup>δ+</sup> a hydride (or a hydride equivalent) from reduced FMN N<sub>5</sub> in TcDHOD.

Dihydroorotate dehydrogenase (DHOD<sup>1</sup>) is a flavoenzyme that catalyzes oxidation of (*S*)-dihydroorotate to orotate, the

fourth step and the only redox reaction in the *de novo* pyrimidine biosynthesis pathway (Figure S1, Supporting Information). In the first half-reaction, oxidation of dihydroorotate is coupled with reduction of a flavin mononucleotide (FMN) cofactor. Based on amino acid sequence similarity, DHODs from different organisms can be divided into two families, family 1 and family 2 (*I*). Family 1 DHODs are cytoplasmic enzymes and can be further subdivided into families 1A and 1B. Family 1A enzymes

<sup>†</sup> This work was supported by grants to S.H. and K.K. from the Targeted Proteins Research Program (TPRP), Japan Aerospace Exploration Agency (JAXA), and in part by Grant-in-Aid for Scientific Research on Priority Areas, for the 21st Century COE Program and Creative Scientific Research from the Japanese Ministry of Education, Culture, Sports and Technology, and for Scientific Research (B) from Japan Society for the Promotion of Science. D.K.I. was a research fellow supported by Japan Society for the Promotion of Science.

<sup>‡</sup> Protein Data Bank coordinates and structure factors have been deposited as entries 2DJX for ligand-free TcDHOD, 2E6F for TcDHOD–oxonate, 2E68 for TcDHOD–dihydroorotate, 2E6A for TcDHOD–orotate, 2E6D for TcDHOD–fumarate and 2DJL for TcDHOD–succinate complexes.

<sup>\*</sup> To whom correspondence should be addressed. K.K.: 7-3-1 Hongo, Bunkyo-ku, Tokyo 113-0033, Japan. Fax: (+81)-3-5841-3526. E-mail: kitak@m.u-tokyo.ac.jp. S.H.: Gogyokaidou-cho, Matsugasaki, Sakyo, Kyoto 606-8585, Japan. Fax: (+81)-75-724-7541. E-mail: harada@kit.ac.jp.

<sup>§</sup> Graduate School of Medicine, The University of Tokyo. Tel: +81-3-5841-3528.

<sup>||</sup> E-mail: danielken@m.u-tokyo.ac.jp.

<sup>‡</sup> Graduate School of Arts and Sciences, The University of Tokyo.

<sup>#</sup> Juntendo University.

<sup>○</sup> Kyoto Institute of Technology. Tel: +81-75-724-7541.

<sup>1</sup> Abbreviations: DHOD, dihydroorotate dehydrogenase; FMN, flavin mononucleotide; FAD, flavin adenine dinucleotide; NAD, nicotinamide adenine dinucleotide; MWCO, molecular weight cutoff.



form homodimers and appear to utilize fumarate as a physiological oxidant, in conjunction with oxidation of the reduced FMN cofactor during the second half-reaction (1). In contrast, family 1B enzymes form heterotetramers and utilize NAD<sup>+</sup> via a distinct protein subunit that contains a 2Fe-2S cluster and FAD cofactor (1). Members of family 2 exist as homodimers or monomers and are membrane-bound enzymes that utilize respiratory quinone as a physiological oxidant during the second half-reaction (2–4). The N-terminal domain found only in family 2 DHODs forms the binding site for quinone (5).

Many inhibitors targeting the quinone binding-site have been designed such as human DHOD inhibitor leflunomide that is in clinical use to treat rheumatoid arthritis (5). Other potent and selective inhibitors designed for family 2 DHODs from *Escherichia coli* (6), *Helicobacter pylori* (7) and *Plasmodium falciparum* (2, 8, 9) inhibit their growth. These inhibitors designed for family 2 DHODs are not effective against family 1A DHODs, since family 1A lacks the quinone binding site. On the other hand, hydroxybenzoates such as 3,4-dihydroxybenzoate and 3,5-dihydroxybenzoate are inhibitors specific for family 1A DHODs (10, 11), although these inhibitors with IC<sub>50</sub>s in the range of micromolar order are not potent. Previously, we reported the organization and amino acid sequences of all enzymes in the *de novo* pyrimidine biosynthesis pathway of *Trypanosoma cruzi* (12). In that work, we found that the *T. cruzi* pyr4 gene product is homologous to family 1A DHODs from *Lactococcus lactis* and *Saccharomyces cerevisiae*. DHOD from *T. cruzi* (TcDHOD) is 313 amino acids in length (Figure 1) and exists in cells as a homodimer (MW 2 × 34 kDa). In addition to DHOD activity, TcDHOD also shows fumarate reductase activity, suggesting that it is involved not only in the *de novo* pyrimidine biosynthesis pathway but also in redox homeostasis of the parasite (12–14). Recently, Annoura et al. (15) demonstrated that TcDHOD knockout *T. cruzi* could not survive even in the presence of substrates for enzymes of pyrimidine salvage pathway. The importance of DHOD to survival of *Trypanosoma brucei* in the blood stream form was also shown by Arakaki et al. (16). Therefore, the enzyme has the characteristics of a promising target for the development of chemotherapeutic agents to combat infections with the pathogen.

To date, X-ray structure analyses have been performed for seven DHODs from six organisms: family 1A DHODs from *L. lactis* (17) and *T. brucei* (16), family 1B DHOD from *L. lactis* (18), and family 2 DHODs from *E. coli* (4), *P. falciparum* (19), *Rattus rattus* (20) and *Homo sapiens* (5). Although kinetic studies of the catalytic mechanism for DHOD have extensively been performed (21–30), none of the structures determined to date include DHOD in a complex with a physiological substrate. In this study, we determined the crystal structures of TcDHOD in the ligand-free form, in complexes with substrates and products of the first and second half-reactions, and in a complex with an inhibitor, oxonate at atomic resolution. These structures, in particular those of TcDHOD complexed with dihydroorotate and fumarate, provided us further insights into the catalytic mechanisms of dihydroorotate oxidation and fumarate reduction.

## EXPERIMENTAL PROCEDURES

**Cloning, Expression and Purification.** Recombinant TcDHOD was expressed, purified and crystallized as previously reported (31). Briefly, TcDHOD was purified to homogeneity using DEAE Fast Flow (GE Healthcare) followed by Phenyl Sepharose H.P. (GE Healthcare) and TSK G3000SW (Tosoh). A total of 11 mg of TcDHOD with high specific activity (12.5 μmol/min/mg) was purified from 10 L of culture (Table S1, Supporting Information). The addition of 0.25 mM orotate during purification and storage was indispensable to stabilize the enzymatic activity.

**Protein Assay and FMN Content Determination.** Protein concentrations were determined according Lowry with bovine serum albumin as the standard (32). The FMN content of the purified TcDHOD was estimated to be 1.0 using a spectroscopic method, on the basis of the extinction coefficient of FMN (11.1 mM<sup>-1</sup> cm<sup>-1</sup> at 450 nm).

**Enzyme Assay.** DHOD activity was measured as described previously (14) with minor modifications. Orotate production was assayed by measuring the absorption at 290 nm ( $\epsilon = 6.4 \times \text{mM}^{-1} \times \text{cm}^{-1}$ ). The reaction was started by adding 0.5 mM dihydroorotate into the reaction mixture containing 50 mM potassium phosphate buffer pH 7.5, 2 mM sodium fumarate and TcDHOD in a final volume of 1 mL.

**Crystallization.** The plate-shaped dark-orange crystals of the TcDHOD–orotate complex with the oxidized FMN cofactor were obtained at 277 K by the hanging drop vapor diffusion method using 16% (w/v) PEG 3350, 100 mM sodium cacodylate pH 6.2, 1 mM sodium orotate, 50 mM hexaamminecobalt (III) chloride and 1 mM sodium thiocyanate as the reservoir solution (31). The TcDHOD–oxonate complex was prepared by repeated concentration and dilution of the purified enzyme with a buffer containing oxonate using an Amicon Ultra-4 10,000 MWCO filter. This was followed by cocrystallization in a similar manner as described above except that cocrystallization was carried out in the presence of 1 mM oxonate instead of orotate at pH 5.1. Crystals of the ligand-free TcDHOD were prepared by back-soaking crystals of the TcDHOD–oxonate complex in buffer A (100 mM cacodylate pH 5.1, 20% (w/v) polyethylene glycol 3350, 50 mM hexaamminecobalt (III) chloride and 1 mM sodium thiocyanate) for three days with repeated buffer exchange. Crystals of the TcDHOD–succinate and –fumarate complexes were prepared by soaking ligand-free crystals for three days in buffer A containing 10 mM succinate or fumarate, respectively. Crystals of the TcDHOD–dihydroorotate complex were obtained by soaking ligand-free crystals for 10 to 15 s in buffer A containing 10 mM dihydroorotate plus 15% (w/v) glycerol. During soaking, the color of the crystals changed from dark to light orange, which indicates that the FMN cofactor was reduced by dihydroorotate. After soaking, a crystal mounted in a nylon loop was immediately flash-frozen in a nitrogen stream at 100 K, and X-ray diffraction data were collected. During data collection, the light orange color of the crystals was kept. Since kinetic analysis indicated that dihydroorotate can be bound to TcDHOD with the reduced FMN cofactor if an excess amount of dihydroorotate is present (14, 26), the crystals prepared should be those of the TcDHOD–dihydroorotate complex with the reduced FMN cofactor.



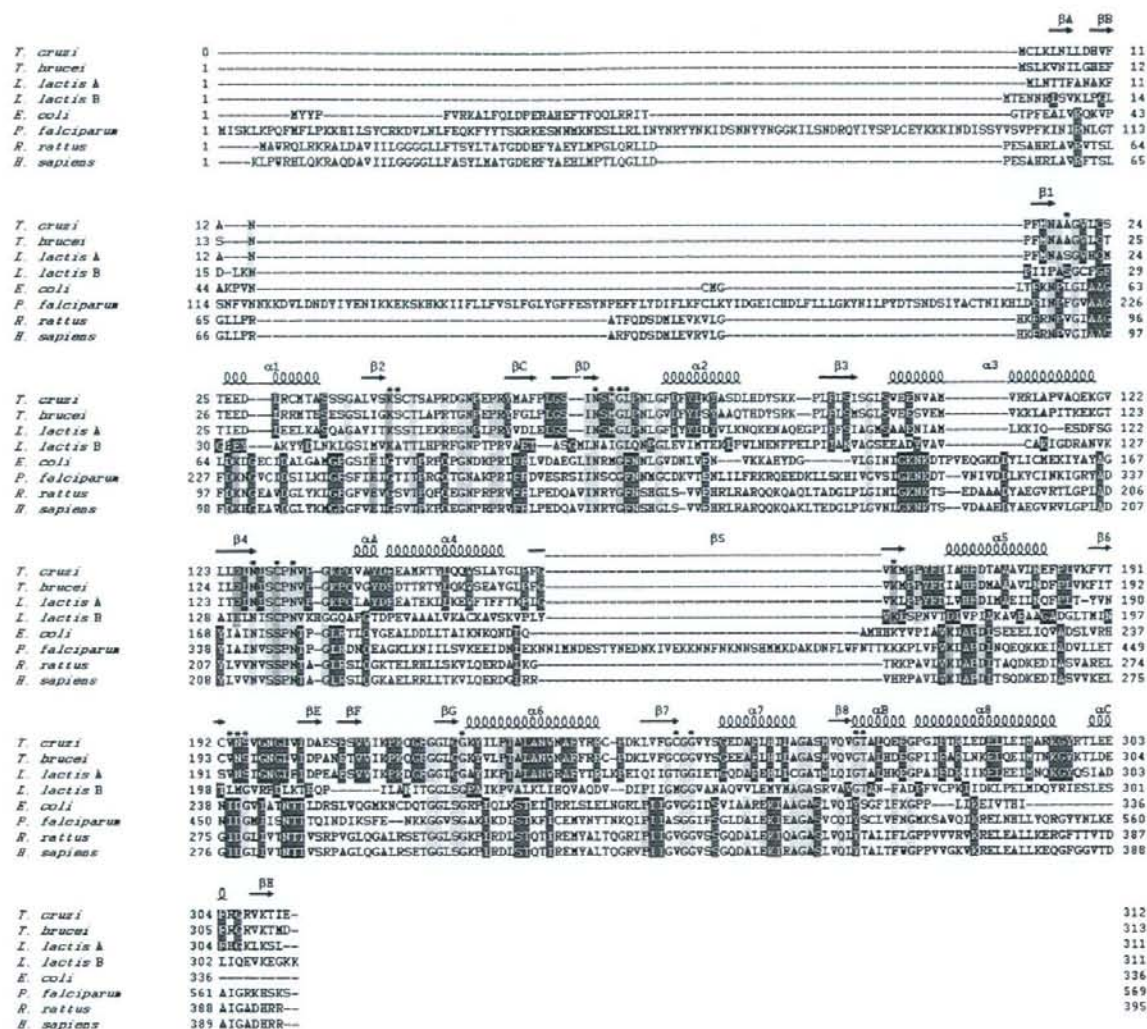


FIGURE 1: Multiple alignment of amino acid sequences of DHODs. The alignment was produced from fourteen amino acid sequences from family 1A (*T. cruzi*/AB212956.1, *T. brucei*/AC159455.1, *L. lactis*/X74206.1, *Streptococcus pneumoniae*/ABJ54983.1 and *Saccharomyces kluyveri*/AY323902.1), catalytic subunit of family 1B (*L. lactis*/CAA52280.1, *Streptococcus thermophilus*/AAV62538.1, *Enterococcus faecalis*/AAO81490, *Clostridium tetani*/AAO36852.1 and *Clostridium cellulolyticum*/ZP\_01576243.1) and family 2 (*E. coli*/CAA26594.1, *P. falciparum*/CAG25203.1, *R. rattus*/CAA56765.1 and *H. sapiens*/AAA50163.1) DHODs using CLUSTAL-W. Alignment of eight DHODs, whose structures are known, is shown. They belong to family 1A (*T. cruzi*, *T. brucei* and *L. lactis* A), family 1B (*L. lactis* B) or family 2 (*E. coli*, *P. falciparum*, *R. rattus* and *H. sapiens*). Their PDB codes are 2DJX (this study), 2B4G (16), 2DOR (29), 1EP2 (18), 1F76 (4), 1TV5 (19), 1UUO (20) and 1D3G (5), respectively. In yellow, residues conserved in more than one family. In red, those conserved only within a family. Secondary structural elements of the TcDHOD structure are also indicated;  $\beta$  strands are shown as arrows and  $\alpha$  helices as squiggles. Residues involved in interactions with FMN, oxonate, dihydroorotate, orotate, fumarate or succinate are marked with an asterisk. TcDHOD Lys43, Glu125, Cys130 and Lys164, which are mentioned in Discussion, along with their structurally equivalent residues in other DHODs, are colored blue. The numbers shown for amino acid residues of the TcDHOD protein referred to those of *L. lactis* DHODA.

**X-ray Data Collection, Phasing and Refinement.** X-ray diffraction data sets for TcDHOD in the ligand-free form and in complexes with orotate, fumarate and succinate were collected at 100 K with beamline BL44XU from SPring-8 ( $\lambda = 0.900 \text{ \AA}$ ) in Harima, Japan, using a Bruker AXS DIP6040 detector. Data sets for TcDHOD-oxonate and -dihydroorotate complexes were collected at 100 K with beamline NW12 of Photon Factory Advanced Ring ( $\lambda = 1.000 \text{ \AA}$ ) in Tsukuba, Japan, using an ADSC Quantum-210 detector. All data sets were indexed, integrated and scaled

using *HKL2000* (33). Table 1 summarizes data collection statistics. The structure of the TcDHOD-orotate complex was solved by the molecular replacement method using *Molrep* (34). A search model was generated from a single monomer of the *L. lactis* DHODA dimer structure (PDB code, 2DOR; 55% sequence identity with TcDHOD) with all non-protein atoms removed. The sequence was changed to that of TcDHOD by applying the TcDHOD sequence (NCBI accession number BAE48283 (35)) onto the search model using *Swiss-Pdb Viewer* (36). The molecular replace-



Table 1: Data Collection and Refinement Statistics<sup>a</sup>

	ligand-free	oxonate	dihydroorotate	orotate	fumarate	succinate
Data Collection						
space group	<i>P</i> 2 <sub>1</sub> 2 <sub>1</sub> 2 <sub>1</sub>	<i>P</i> 2 <sub>1</sub> 2 <sub>1</sub> 2 <sub>1</sub>	<i>P</i> 2 <sub>1</sub> 2 <sub>1</sub> 2 <sub>1</sub>	<i>P</i> 2 <sub>1</sub> 2 <sub>1</sub> 2 <sub>1</sub>	<i>P</i> 2 <sub>1</sub> 2 <sub>1</sub> 2 <sub>1</sub>	<i>P</i> 2 <sub>1</sub> 2 <sub>1</sub> 2 <sub>1</sub>
cell dimensions <i>a</i> , <i>b</i> , <i>c</i> (Å)	69.96, 73.13, 126.09	68.36, 71.83, 123.64	68.44, 71.94, 123.85	68.25, 71.88, 123.57	68.28, 71.88, 123.61	68.15, 71.77, 123.40
wavelength (Å)	0.9	1.0	1.0	0.9	0.9	0.9
resolution (Å)	50.0–1.58 (1.64–1.58)	50.0–1.26 (1.29–1.26)	50.0–1.38 (1.43–1.38)	50.0–1.64 (1.70–1.64)	50.0–1.94 (2.01–1.94)	50.0–1.38 (1.43–1.38)
<i>R</i> <sub>merge</sub> (%)	7.0 (39.8)	7.1 (39.5)	8.4 (39.6)	7.8 (39.8)	9.9 (24.4)	6.0 (33.0)
<i>I</i> / <i>σ</i> ( <i>I</i> )	8.2 (2.76)	8.5 (3.04)	10.5 (4.26)	9.9 (3.12)	12.8 (8.19)	9.0 (2.62)
completeness (%)	98.5 (99.4)	97.7 (99.2)	97.5 (98.9)	96.1 (97.9)	99.9 (100.0)	94.9 (69.5)
redundancy	4.0	4.4	4.6	3.7	6.1	5.2
Refinement						
resolution (Å)	40.0–1.58	30.0–1.26	30.0–1.38	50.0–1.64	50.0–1.94	50.0–1.38
no. of reflections	86263	152389	116503	68521	43381	112910
<i>R</i> -factor/ <i>R</i> -free	0.182/0.204	0.166/0.180	0.169/0.183	0.164/0.192	0.158/0.200	0.166/0.183
no. of atoms						
protein	4758	4758	4758	4758	4758	4758
FMN	31	31	31	31	31	31
ligand	0	22	22	22	16	16
water	689	799	637	497	476	696
<i>B</i> -factors						
protein	17.1	9.9	12.0	10.7	9.7	12.0
FMN	11.5	5.7	4.5	6.1	5.1	7.4
ligand		6.8	7.4	5.6	11.8	9.6
water	25.0	19.6	18.0	20.9	17.5	21.2
rms deviations						
bond lengths (Å)	0.009	0.007	0.008	0.011	0.015	0.007
bond angles (deg)	1.219	1.171	1.219	1.309	1.438	1.192

<sup>a</sup> Highest-resolution shell is shown in parentheses.

ment was carried out under different resolution ranges of 2.0–8.0, 3.0–8.0 and 4.0–8.0 Å. Essentially consistent solutions giving one TcDHOD dimer in the asymmetric unit were obtained. The resulting model obtained after rigid-body refinement was refined at 2.5 Å resolution under strict noncrystallographic symmetry (NCS) restraints using *CNS* (37), and electron-density maps calculated with  $\sigma_A$ -weighted  $2F_o - F_c$  and  $F_o - F_c$  coefficients were generated and inspected to check the validity of the initial model. After a few rounds of refinement and manual rebuilding using *CNS* and *Coot* (38), respectively, FMN cofactors and orotate molecules became clearly visible on electron-density maps and were incorporated into the model. Subsequently, the model was subjected to iterative cycles of refinement and manual rebuilding at 1.64 Å resolution using isotropic temperature factors and weak NCS restraints. At this stage, many water molecules were identified using electron-density maps ( $3\sigma$  cutoff). The model was finally refined using *Refmac5* (39) and *Coot* without NCS restraints, resulting in *R*-factor and *R*-free values of 0.164 and 0.192, respectively. In the final homodimer model of the TcDHOD–orotate complex, each subunit consists of 312 amino acid residues from Met0 to Ile311, one oxidized FMN cofactor and one orotate molecule. The C-terminal amino acid residue, Glu312, could not be defined on the final  $2F_o - F_c$  electron density map. In the Ramachandran plot (40), 93.2% of the residues are in the most favored regions and 6.8% are in additionally allowed regions, as defined by *PROCHECK* (41). The structures of the ligand-free TcDHOD and the complexes with dihydroorotate, oxonate, fumarate and succinate were refined starting from the protein atom coordinates of the TcDHOD–orotate complex. Coordinate files and

appropriate restraints for those ligands were generated using the PRODRG server and Sketcher program of the CCP4 suite (42).

Successful preparations of crystals of the ligand-free TcDHOD and those of TcDHOD in complexes with dihydroorotate, fumarate and succinate were confirmed by inspecting  $2F_o - F_c$  electron density maps calculated after omit refinement (Figure S2 A–L, Supporting Information). In the map calculated for the ligand-free TcDHOD (Figure S2 A, B), four water molecules located near the FMN isoalloxazine ring in the active site were assigned. Well-shaped electron dense regions corresponding to dihydroorotate, fumarate or succinate were also recognized in the active site of each complex. Refinement statistics for all models are summarized in Table 1.

## RESULTS

**Overall Structure.** In the presence of orotate, the TcDHOD protein, consisting of 313 amino acid residues and one oxidized FMN cofactor, was crystallized in orthorhombic space group *P*2<sub>1</sub>2<sub>1</sub>2<sub>1</sub> with two identical subunits related by a noncrystallographic 2-fold axis present in the crystallographic asymmetric unit. Crystals of the ligand-free TcDHOD and of TcDHOD in complexes with the substrates (dihydroorotate and fumarate), products (orotate and succinate) and the inhibitor (oxonate) were prepared as described in Experimental Procedures. Crystals of TcDHOD–dihydroorotate complex included the reduced FMN cofactor, but the other five crystal forms included the oxidized FMN cofactor. All structures determined included a 312 amino acid region from Met0 to Ile311 of the full-length protein but the C-terminal Glu312 was not assigned. Figure 1 shows a multiple amino acid sequence alignment of TcDHOD and



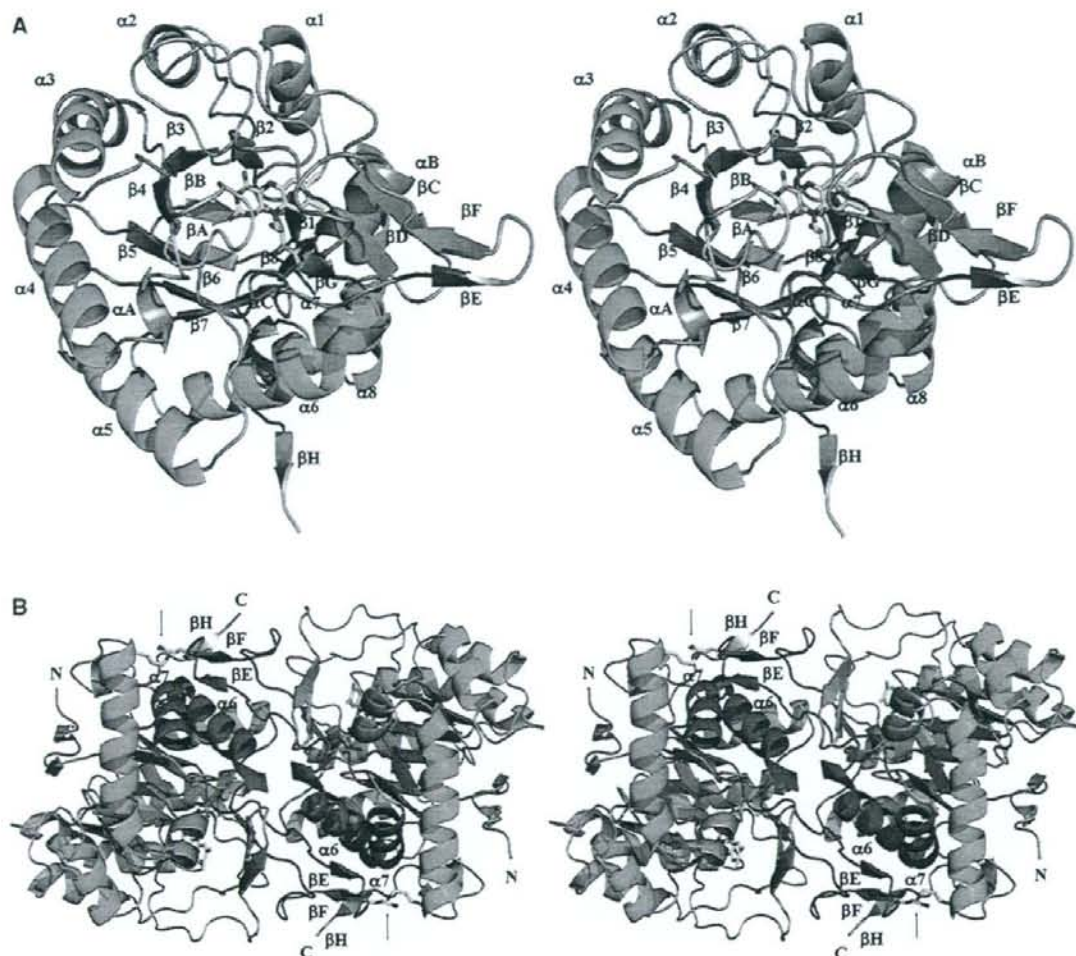


FIGURE 2: Structure of ligand-free TcDHOD (stereo views). (A) Ribbon diagram of the TcDHOD subunit structure. The  $(\alpha/\beta)_8$  barrel is represented in blue ( $\alpha$ -helices) and magenta ( $\beta$ -strands); the  $\beta_4$ - $\alpha_A$  loop, the active site loop, is shown in gray; and the FMN cofactor is shown in yellow. The color code for each atom type is as follows: red, oxygen; blue, nitrogen; orange, phosphate. The same color-code was applied to all figures. (B) The dimer structure viewed from above the 2-fold axis. The  $(\alpha/\beta)_8$  barrel of each subunit is color-coded as described in (A). The  $\beta_6$ - $\alpha_6$  loops, helices  $\alpha_6$  and  $\alpha_7$ , which participate in dimer interface interactions, are in red. Arrows indicate intersubunit salt bridges between Glu207 and Lys296, shown in yellow. The images were generated using PyMOL (<http://pymol.sourceforge.net>).

seven DHODs with known structures. Figures 2A and 2B show the subunit and homodimer structures of the ligand-free TcDHOD. As there are no significant differences between the structures of the two subunits, as indicated by a root-mean-square (rms) deviation of 0.20 Å calculated for superimposed 312  $C_\alpha$  positions, we will instead focus on one subunit to describe the structure as a whole.

The overall structure of TcDHOD is very similar to those of other DHODs listed in Figure 1. The  $C_\alpha$  atoms of a TcDHOD subunit can be superimposed on the structurally equivalent 311  $C_\alpha$  atoms of *T. brucei* DHOD (PDB code, 2B4G) or the 298  $C_\alpha$  atoms of *L. lactis* DHODA (2DOR) with rms deviations of 0.39 and 0.82 Å, respectively, which indicates that the main-chain structures of these three DHODs, especially TcDHOD and *T. brucei* DHOD, are essentially identical. The rms deviations for DHODs from different families are somewhat larger; namely, for the family 1B member *L. lactis* DHODB (1EP2), rms deviation of 1.94

Å for 270  $C_\alpha$  atoms and for family 2 members, as follows, 1.76 Å for 253  $C_\alpha$  atoms of *E. coli* DHOD (1F76), 1.68 Å for 275  $C_\alpha$  atoms of *P. falciparum* DHOD (1TV5), 1.81 Å for 186  $C_\alpha$  atoms of *R. rattus* DHOD (1UUO) and 1.74 Å for 272  $C_\alpha$  atoms of *H. sapiens* DHOD (1D3G). In addition, the dimer structure of DHOD from *T. cruzi* Y strain, in which TcDHOD Phe61 is replaced by a valine residue, was determined at 2.2 Å resolution as a form with a sulfate ion bound to its active site (43); PDB code 3C3N, during the submission of this article. TcDHOD is very similar to 3C3N as indicated by the rms deviation of 0.44 Å.

As is true for the many other flavin containing proteins, TcDHOD subunits fold into an  $(\alpha/\beta)_8$  motif with a parallel eight-stranded  $\beta$ -barrel ( $\beta_1$ - $\beta_8$ ) surrounded by eight  $\alpha$ -helices ( $\alpha_1$ - $\alpha_8$ ), with the FMN cofactor on the C-terminal end of the  $\beta$ -barrel. Each of the secondary structural elements of the  $(\alpha/\beta)_8$  motif is connected to the next one via a short loop consisting of several amino acid residues. The loops



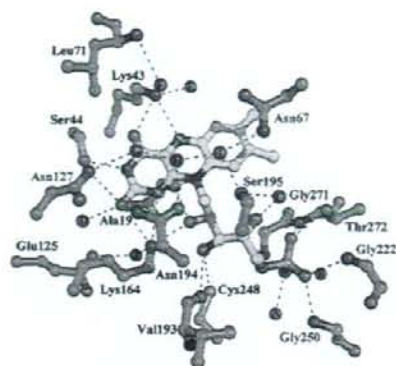


FIGURE 3: The environment of the FMN cofactor of the ligand-free TcDHOD. Amino acid residues and the FMN cofactor are indicated by green or yellow ball-and-stick models, respectively, and ten water molecules (A–J) that were assigned in this region are also shown. Hydrogen bonds are represented by dotted lines. Residue names shown by red are conserved in the amino acid sequences of all known DHODs. The images were generated using PyMOL (<http://pymol.sourceforge.net>).

connecting  $\beta 2$  and  $\alpha 2$  ( $\beta 2$ – $\alpha 2$  loop, residues 43–75),  $\beta 4$  and  $\alpha 4$  ( $\beta 4$ – $\alpha 4$  loop, residues 128–142) and  $\beta 6$  and  $\alpha 6$  ( $\beta 6$ – $\alpha 6$  loop, residues 193–222) are longer than the others and include additional secondary structural elements. Moreover, in each subunit,  $\beta C$ ,  $\beta D$  in the  $\beta 2$ – $\alpha 2$  loop and  $\beta G$  in the  $\beta 6$ – $\alpha 6$  loop form a three-stranded antiparallel  $\beta$ -sheet, whereas  $\beta E$  and  $\beta F$  in the  $\beta 6$ – $\alpha 6$  loop form a two-stranded antiparallel  $\beta$ -sheet (Figure 2A). In the dimer structure, the  $\beta 6$ – $\alpha 6$  loop protrudes from one subunit toward  $\alpha 6$  and  $\alpha 7$  of the other, forming dimer interfaces. Each interface includes an intersubunit three-stranded  $\beta$ -sheet composed of  $\beta E$  and  $\beta F$  of one subunit plus  $\beta H$  of the other, and an intersubunit salt bridge between Glu207 and Lys296 (Figure 2B). Additionally, hydrophobic interactions occur between subunits.

The FMN cofactor is well buried except for a partially exposed dimethyl benzene moiety. One side of the FMN isoalloxazine ring faces toward the C-terminal end of the barrel, and the other side is veiled in three long  $\beta 2$ – $\alpha 2$ ,  $\beta 4$ – $\alpha 4$  (residues 128–138) and  $\beta 6$ – $\alpha 6$  loops. In particular, the  $\beta 4$ – $\alpha 4$  loop, which includes an amino acid sequence that is highly conserved among all DHODs (Figure 1) and has been identified as the active site loop in *L. lactis* DHODA (22, 28) and *E. coli* DHOD (44), is located just over the FMN cofactor, preventing an outside solvent from contacting the isoalloxazine ring (Figure 2A). Figure 3 shows amino acid residues and bound water molecules in the FMN cofactor region. Nitrogen and oxygen atoms of the isoalloxazine ring interact via hydrogen bonds with Ala19 O, Lys43 N<sub>ε</sub>, Ser44 O, Asn127 N<sub>δ2</sub>, Lys164 N<sub>ε</sub> and water D, but the hydrophobic dimethyl benzene moiety lacks close contacts with amino acid residues of TcDHOD. In addition, ribityl hydroxyl groups interact with Ala19 O, Lys164 N<sub>ε</sub>, Val193 O, Cys248 S<sub>γ</sub> and water C, and the phosphate group interacts with main chain imino nitrogen atoms of Gly222, Gly250, Gly271 and Thr272 as well as Thr272 O<sub>γ1</sub>, water A and B. Three hydrogen bonds formed between Lys164 and the isoalloxazine should play a crucial role in binding FMN to TcDHOD, as indicated by the K164A mutant of *L. lactis* DHODA, to which FMN does not bind (22). The negative charge on the phosphate group seems to be

stabilized by hydrogen bonds with these main chain imino nitrogen atoms, as has been observed for the oxyanion holes of serine proteases (45). There are four water molecules (F, G, H and I) in each cavity formed between the isoalloxazine ring and the  $\beta 4$ – $\alpha 4$  loop. Three water molecules interact with one another and with Asn67 N<sub>δ2</sub>, Leu71 N, Asn127 N<sub>δ2</sub>, Asn194 O<sub>δ1</sub> and Ser195 O<sub>γ</sub>. Most of the amino acid residues referred to here have been completely or well conserved in all known DHOD sequences and participate in interactions with FMN cofactors in the structures of DHODs listed in Figure 1.

**Binding of Dihydroorotate, Orotate and Oxonate to TcDHOD.** (S)-Dihydroorotate, orotate and oxonate are a substrate, product and competitive inhibitor of DHODs, respectively (21). Figures 4A–C show that each of these compounds binds to the cavity in the same manner, at the position occupied by waters F, G, H and I in the ligand-free structure. Correspondingly, O8, O4, N3 and O2 of each compound are positionally related to waters F, G, H and I, respectively. In the bound form, orotate and oxonate are in a planar conformation with the exception of their carboxyl oxygen atoms. For dihydroorotate, by contrast, C5 and C6 deviate from the plane constituted by N1, C2, N3, C4, O2 and O4 at a distance and direction of 0.20 Å away from or 0.29 Å toward the isoalloxazine ring, respectively. The dihydroorotate carboxyl group is in an equatorial conformation and faces away from the isoalloxazine ring, whereas the calculated position of the axial C6 hydrogen, H6, is located between C6 and FMN N5 (Figure 4A).

The bound dihydroorotate, orotate and oxonate stack parallel to the isoalloxazine ring and do not appear to cause any discernible changes in the conformation of the TcDHOD polypeptide as compared with the ligand-free form. These compounds interact via hydrogen bonds with Lys43 N<sub>ε</sub>, Asn67 O<sub>δ1</sub> and N<sub>δ2</sub>, Gly70 N, Asn127 N<sub>δ2</sub>, Asn132 N<sub>δ2</sub>, Asn194 O<sub>δ1</sub> and N<sub>δ2</sub>, Met69 N, Leu71 N and Ser195 O<sub>γ</sub>. The carboxyl groups of dihydroorotate, orotate and oxonate are twisted about their C<sub>6</sub>–C<sub>7</sub> bonds with C<sub>5</sub>–C<sub>6</sub>–C<sub>7</sub> dihedral angles of 98.5°, 127.0° and 113.2°, respectively. Their carboxyl O<sub>8</sub> atoms interact with Lys43 N<sub>ε</sub> and Leu71 N, and their carboxyl O<sub>9</sub> atoms with Gly70 N, Met69 N and Asn132 N<sub>δ2</sub> (Figures 4A–C). Interactions that involve protein nitrogen atoms are commonly found in the structures of other DHOD–orotate complexes, and seem to be involved in stabilization of negative charges on their carboxyl groups and of the twisted conformation.

Cys130 in the  $\beta 4$ – $\alpha 4$  loop, which has previously been identified as the catalytic base in *L. lactis* DHODA (21–23, 28, 29), is located with its S<sub>γ</sub> at distances of 3.52 Å, 4.94 Å and 4.46 Å from dihydroorotate C<sub>5</sub>, O<sub>8</sub> and O<sub>9</sub>, respectively. Nearly equal distances were also determined for the distance between S<sub>γ</sub> and orotate C<sub>5</sub>, O<sub>8</sub> and O<sub>9</sub> (that is, 3.62 Å, 4.92 Å and 4.66 Å, respectively). In both cases, the distance from S<sub>γ</sub> to O<sub>8</sub> or O<sub>9</sub> is too far for the thiol group to interact with either, according to the van der Waals radii for SH (2.34 Å) and O (1.40 Å) (46). However, the distances between S<sub>γ</sub> and C<sub>5</sub> are favorable for a S<sub>γ</sub>···H–C<sub>5</sub> interaction in the bound dihydroorotate, and for a S<sub>γ</sub>–H···C<sub>5</sub> interaction in the bound orotate (Figures 4A,B).

Oxonate, a competitive inhibitor for all DHODs (21) (IC<sub>50</sub> = 35 μM for TcDHOD), appears to be bound to TcDHOD in the same manner observed for dihydroorotate and orotate



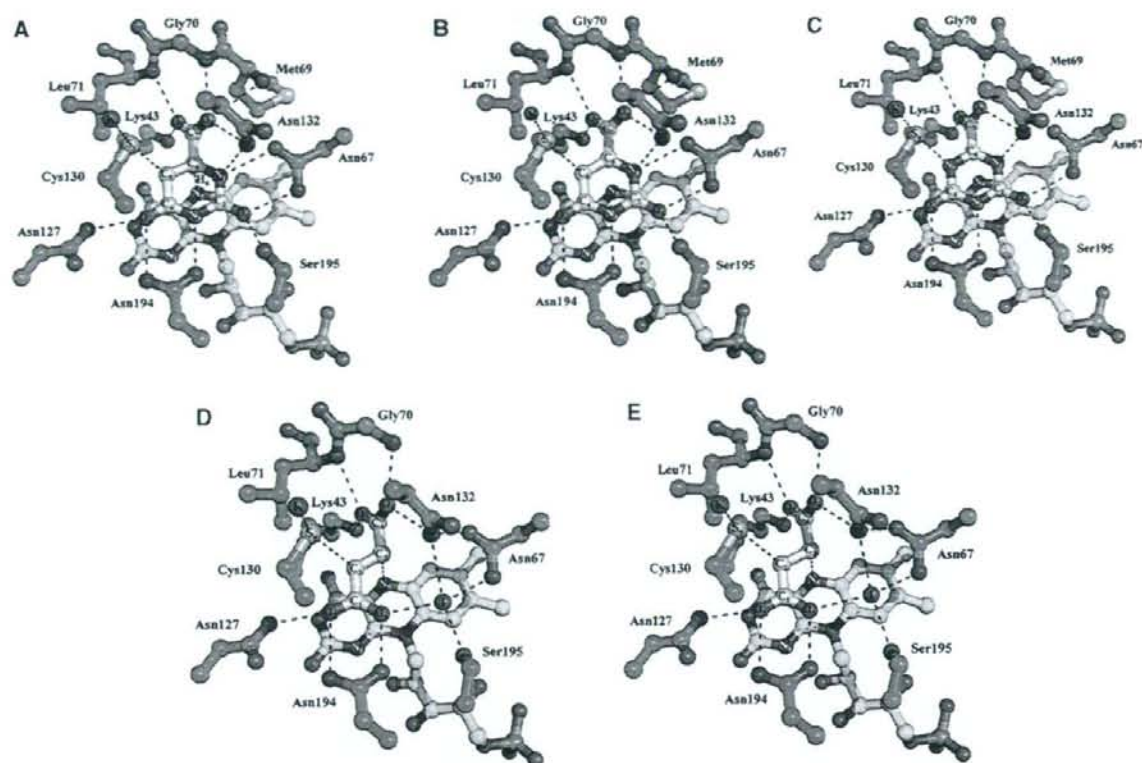


FIGURE 4: Binding of (A) dihydroorotate, (B) orotate, (C) oxonate, (D) fumarate and (E) succinate to TcDHOD. Amino acid residues, FMN and bound compounds are shown as green, yellow or white ball-and-stick models, respectively. The substrates and products of the first half-reaction (dihydroorotate and orotate) and second half-reaction (fumarate and succinate) and a competitive inhibitor (oxonate) are bound to TcDHOD in a similar manner. In (A)–(E), Cys130  $S_{\gamma}$  forms a hydrogen bond with water K and is located 3.52 Å, 3.62 Å, 3.42 Å, 3.43 Å and 3.60 Å from dihydroorotate  $C_5$ , orotate  $C_5$ , oxonate  $N_5$ , fumarate  $C_2$  and succinate  $C_2$ , respectively. The FMN  $N_5$  is located 3.25 Å, 3.65 Å, 3.66 Å, 3.51 Å and 3.32 Å from dihydroorotate  $C_6$ , orotate  $C_6$ , oxonate  $C_6$ , fumarate  $C_3$  and succinate  $C_3$ , respectively. In each structure, possible hydrogen bond interactions are shown only for those between the compounds and TcDHOD, and are represented by dotted lines. The images were generated with PyMOL (<http://pymol.sourceforge.net>).

(Figure 4C). The distances between oxonate  $O_9$  and Met69 N, oxonate  $N_1$  and Asn67  $O_{\beta 2}$  are longer by 0.28–0.46 Å than those observed in the bound dihydroorotate and orotate. However, an additional hydrogen bond with a distance of 3.41 Å is formed between oxonate  $N_5$  and Cys130  $S_{\gamma}$ . This interaction probably contributes to a decrease in the average  $B$ -factor of the main-chain atoms of the  $\beta 4$ – $\alpha A$  loop to 6.9 Å<sup>2</sup> as compared with 9.4 Å<sup>2</sup> and 15.0 Å<sup>2</sup> for the TcDHOD–dihydroorotate and –orotate complexes, respectively, and thus, to suppression of the flexibility of the  $\beta 4$ – $\alpha A$  loop.

**Binding of Fumarate and Succinate to TcDHOD.** Both fumarate and succinate are bound to the same site as dihydroorotate, orotate and oxonate via identical hydrogen bonds with TcDHOD amino acid residues (Figures 4D,E). The bound fumarate and succinate are in a planar conformation, approximately parallel to the isoalloxazine ring, with the exception of the second carboxyl  $O_3$  and  $O_4$  atoms. As observed in the bound dihydroorotate, orotate and oxonate, the second carboxyl groups are twisted about the  $C_3$ – $C_4$  bonds with  $C_2$ – $C_3$ – $C_4$ – $O_4$  dihedral angles of 99.1° and 92.4°, respectively, and interact with protein nitrogen atoms. On the other hand, the first carboxyl  $C_1$ ,  $O_1$  and  $O_2$  atoms occupy the  $C_4$ ,  $O_4$  and  $N_3$  positions, respectively, of the bound dihydroorotate *etc.*

$C_2$  and  $C_3$  of the bound fumarate and succinate are in close contact with Cys130  $S_{\gamma}$  and FMN  $N_5$ , respectively. The distances between  $S_{\gamma}$  and  $C_2$  are 3.43 and 3.60 Å for the bound fumarate and succinate, respectively, and those between  $N_5$  and  $C_3$ , 3.51 and 3.32 Å. Accordingly,  $S_{\gamma}$  and  $C_2$ , as observed in the bound dihydroorotate *etc.*, are also at a distance favorable for a  $S_{\gamma}$ –H $\cdots$  $C_2$  interaction in the bound fumarate, and for a  $S_{\gamma}$ –H $\cdots$  $C_2$  interaction in the bound succinate (Figures 4D,E).

## DISCUSSION

In this study, we determined, at atomic resolution, the structures of TcDHOD in the ligand-free form and in complexes with physiological substrates (dihydroorotate and fumarate) and reaction products (orotate and succinate), as well as in a complex with the competitive inhibitor oxonate. We found that the substrates and products of the first and the second half-reactions bind to the same site of TcDHOD, which is consistent with the one-site ping-pong Bi-Bi mechanism demonstrated by kinetic studies for family 1A DHODs (14, 26, 27, 47). The structures of each of the five complexes can be superimposed on the ligand-free structure with an rms deviation in the range 0.11 Å to 0.13 Å for subunit 312  $C_{\alpha}$  positions, and 0.12 Å to 0.16 Å for dimer



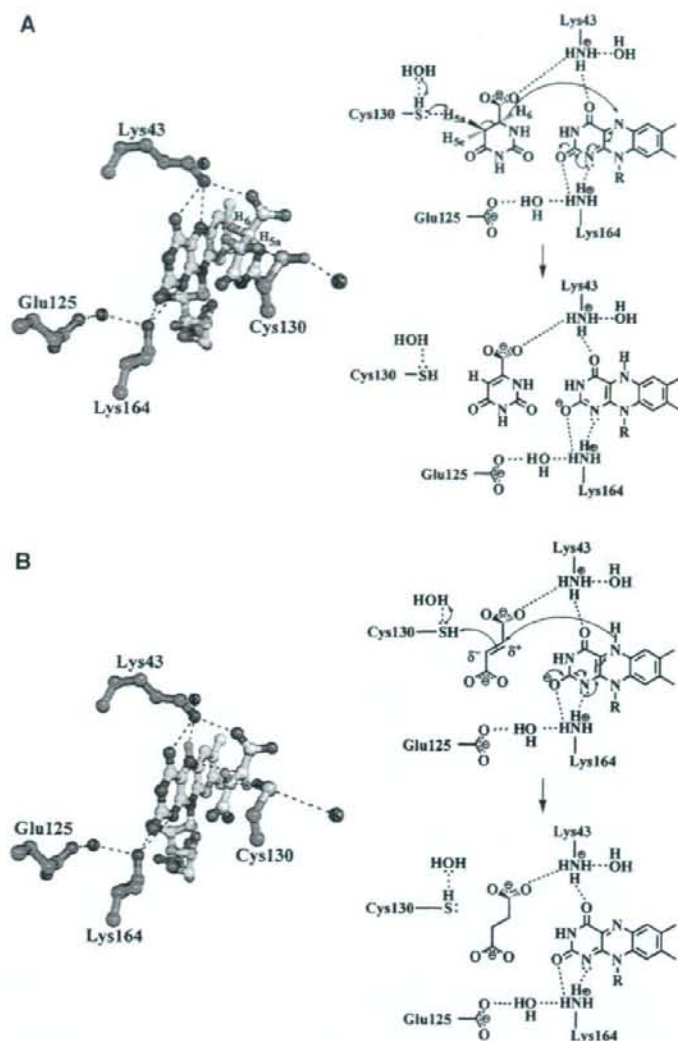


FIGURE 5: Proposed mechanisms for (A) the first half-reaction (oxidation of dihydroorotate to orotate) and (B) the second half-reaction (reduction of fumarate to succinate) as carried out by TcDHOD. The FMN cofactor (yellow), amino acid residues (green) and substrates (white) are represented using ball-and-stick models drawn with PyMOL. The hydrogen atoms of dihydroorotate C5, C6 and Cys130S $\gamma$  are shown at their calculated positions (cyan balls).

624 C $\alpha$  positions. Furthermore, in each structure we determined, both the oxidized and the reduced FMN cofactors are essentially planar, and the FMN cofactor and its peripheral 72 amino acid residues within 8 Å can be superimposed on the ligand-free form, with an rms deviation of 0.06 Å to 0.10 Å between subunits, and 0.08 Å to 0.11 Å between dimers. Thus, the protein and FMN cofactor portions of the complexes are essentially identical with the ligand-free TcDHOD. Although structures determined in this study do not reveal physiological states in the sense that orotate and fumarate bind to TcDHOD with the oxidized FMN cofactor and dihydroorotate binds to TcDHOD with reduced FMN, they should be good models for the TcDHOD enzymatic reaction pathway. On the basis of the X-ray crystal structures determined in this study, here we discuss the mechanisms of the first and the second half-reactions brought about by TcDHOD.

*Structural Insight into the First Half-Reaction, Dihydroorotate Oxidation.* The mechanism of the first half-reaction has been extensively discussed based on kinetic analyses (21, 23, 24, 26, 47) and crystal structures (17, 18, 28, 29), and Cys130 has been identified as the active site base for *L. lactis* DHODA that abstracts a proton from dihydroorotate C5. In the crystal structure of the TcDHOD–dihydroorotate complex, Cys130 S $\gamma$  is 3.52 Å and 3.59 Å away from dihydroorotate C5 and water K, respectively (Figure 5A). In addition, the calculated positions of the axial C5 hydrogen, H<sub>5a</sub>, and Cys130 S $\gamma$  hydrogen, H<sub>5</sub>, are favorably disposed for the H<sub>2</sub>O<sup>K</sup>...H<sub>5</sub>–S $\gamma$ ...H<sub>5a</sub>–C5 interaction, as indicated by the distances S $\gamma$ –H<sub>5a</sub> (2.54 Å) and H<sub>5</sub>–O<sup>K</sup>H<sub>2</sub> (2.32 Å), and by the angles S $\gamma$ –H<sub>5a</sub>–C5 (157.5°) and S $\gamma$ –H<sub>5</sub>–O<sup>K</sup>H<sub>2</sub> (148.8°). The water K is linked to outside solvents through a hydrogen bond chain formed by three water molecules that are located in a hydrophilic channel connecting Cys130S $\gamma$



to the outside. This channel is also found in family 1A DHODs (2B4G and 2DOR), but it is not found in the K213E mutant of *L. lactis* DHODA (1JQV), in which the active site loop closes the channel. Family 1B DHOD from *L. lactis* (1EP2) does not have this hydrophilic channel; instead, the active site Cys135 is on the molecular surface. Because of this exquisite disposition of Cys130 and the hydrogen bond chain, dihydroorotate  $H_{5a}$  would be abstracted by Cys130 as a proton and then relayed to an outside solvent through the hydrogen bond chain.

Together with the proton abstraction from  $C_5$ , dihydroorotate  $H_6$  is transferred to FMN  $N_5$  as a hydride (or a hydride equivalent) to reduce the cofactor. As mentioned above in the Results section, the calculated position of  $H_6$  (between  $C_6$  and FMN  $N_5$ , 2.19 Å away from FMN  $N_5$ , with a  $C_6-H_5-N_5$  angle of  $160^\circ$ ) is suitably disposed for the hydride transfer. The structure of the TcDHOD-dihydroorotate complex shows that the reduced FMN cofactor is essentially planar, which indicates that it is not neutral reduced FMN, FMNH<sub>2</sub>, but anionic reduced FMN, FMNH<sup>-</sup> (48). The negative charge of the anionic reduced FMN is stabilized by Lys43 and Lys164 (Figure 5A). Lys164 is part of the hydrogen bond network of Glu125...H<sub>2</sub>O...Lys164...FMN. Although both Glu125 and Lys164 are shielded from outside solvents, a proton would be shifted from the Glu125 carboxyl group to the Lys164 amino group through the hydrogen bond network. Both of the residues are conserved only in the amino acid sequences of DHODs from families 1A and 1B (Figure 1), but inspections of the crystal structures of family 2 DHODs show that alternative glutamate and lysine residues conserved in amino acid sequences of family 2 DHODs (for example, *H. sapiens* DHOD Glu116 and Lys255) similarly form the hydrogen bond network of Glu116...H<sub>2</sub>O...Lys255...FMN.

In summary, the first half-reaction proceeds as follows (Figure 5A). After binding of dihydroorotate to TcDHOD, a hydride (or a hydride equivalent) is transferred from dihydroorotate  $C_6$  to FMN  $N_5$ , and Cys130  $S_\gamma$  completes oxidation of dihydroorotate by abstracting a proton from  $C_5$ , which is relayed to an outside solvent via the H<sub>2</sub>O<sup>K</sup>...H<sub>5</sub>-S<sub>γ</sub>...H<sub>5a</sub>-C<sub>5</sub> network. The negative charge of the anionic reduced FMN is stabilized by Lys43 and Lys164. This mechanism is consistent with previous works (18, 23–26, 28–30). Although we cannot be sure whether the scission of  $C_6-H_6$  and  $C_5-H_{5a}$  bonds is concerted or stepwise, and we cannot be sure whether  $H_6$  is transferred to FMN  $N_5$  as a hydride or a hydride equivalent, the concerted mechanism with the transfer of a hydride equivalent has been proposed for family 1 DHODs (23).

**Structural Insight into the Second Half-Reaction, Fumarate Reduction.** Unlike the physiological substrate of the first half-reaction, those of the second half-reaction differ among the DHOD subfamilies. The reduced FMN cofactor for TcDHOD converts fumarate to succinate, whereas NAD<sup>+</sup> is reduced to NADH by family 1B DHODs, and ubiquinone is reduced to ubiquinol by family 2 DHODs.

The prominent feature we found in the TcDHOD-fumarate complex is that the conformation of the bound fumarate is nonplanar. The second carboxyl group is twisted around the  $C_3-C_4$  bond with a  $C_2-C_3-C_4-O_4$  dihedral angle of  $99.1^\circ$  as observed in the bound succinate, dihydroorotate, orotate and oxonate structures. The bound fumarate is twisted by

interactions with Lys43  $N_\epsilon$ , Leu71  $N$ , Gly70  $N$ , and Asn132  $N_{\delta 2}$  (Figure 4D). Twisting around the  $C_3-C_4$  bond breaks the uniform distribution of  $\pi$ -electrons over the conjugated double bonds of fumarate, and partial charge separation, represented as  $C_2^{\delta-}$  and  $C_3^{\delta+}$ , is then induced. Together with the shorter distances of  $C_2^{\delta-}-Cys130 S_\delta$  (3.43 Å) and  $C_3^{\delta+}-FMN N_5$  (3.15 Å) than those of  $C_3^{\delta+}-Cys130 S_\delta$  (4.24 Å) and  $C_2^{\delta-}-FMN N_5$  (4.03 Å), this partial charge separation may act as a guide, leading a hydride (or hydride equivalent) from FMN  $N_5$  to  $C_3^{\delta+}$  and a proton from Cys130  $S_\gamma$  to  $C_2^{\delta-}$  in the thermodynamically favorable reduction of fumarate with reduced FMN. In the same manner as the TcDHOD-dihydroorotate complex, the water K (Figure 5B) was also in the  $2F_o - F_c$  electron density map of the TcDHOD-fumarate complex (Supporting Information Figure S2J), and acts a part of the hydrogen bond network HO<sup>K</sup>-H...S<sub>γ</sub>-H<sub>5</sub>...C<sub>2</sub><sup>δ-</sup>. Therefore, a proton can be relayed from an outside solvent to  $C_2^{\delta-}$  through the network (Figure 5B).

To find out whether this fumarate twisting is common, we searched the Protein Data Bank for protein structures with fumarate. Ten structures were found. Four [1D4E (49), 1P2E (50), 2BS2 (51), and 1QLB (52)] are flavoproteins with fumarate reductase activity, and six [1PJ2 (53), 1QCO (54), 2CGO (55), 2EEO (not published), 2PTQ (56), and 2VD6 (not published)] are enzymes in which fumarate is a product (1QCO, 2PTQ, 2VD6), an inhibitor (2CGO, 2EEO), or an allosteric activator (1PJ2). Twisted fumarate is near the isoalloxazine in all fumarate reductases except 2BS2, while a planar fumarate is bound to the other six. Unlike TcDHOD, the distances between  $C_2^{\delta-}$  and  $N_5$  (3.38 to 3.96 Å) are comparable with those between  $C_3^{\delta+}$  and  $N_5$  (3.35 to 3.89 Å) in 1D4E, 1P2E and 1QLB. Both 2BS2 and 1QLB are quinol:fumarate oxidoreductase from *Wolinella succinogenes*, but 2BS2, in which the active site loop is half-open, is probably unreactive. While the number of examples is small, we speculate that the twisting of fumarate is common in flavoproteins with fumarate reductase activity.

In summary, at atomic resolution we determined the three-dimensional structures of TcDHOD in ligand-free form and in complexes with dihydroorotate, orotate, oxonate, fumarate, and succinate. All structures are essentially identical and include a planar FMN cofactor. The planar reduced FMN cofactor of TcDHOD-dihydroorotate complex indicates that the cofactor is in the form of the anionic reduced FMN. Taking these structures as models of the enzymatic pathway gives insight regarding the catalytic mechanisms of dihydroorotate oxidation and fumarate reduction. We expect that information about the structure of TcDHOD obtained in this study, particularly about interactions between the enzyme and the inhibitor and physiological substrates, will be useful in the design specific and effective inhibitors against TcDHOD.

#### ACKNOWLEDGMENT

We thank all staff members at beamlines BL44XU at Spring-8 and NW12 at Photon Factory for their help with X-ray diffraction data collection and T. Nakazawa (Nara Women's University) for helpful discussions.



## SUPPORTING INFORMATION AVAILABLE

One purification table of recombinant TcDHOD (Table S1), a figure (S1) explaining the pyrimidine *de novo* biosynthesis as well as fumarate and succinate metabolism in *T. cruzi* and a figure (S2) showing detailed electron density map of all ligands complexed with TcDHOD. This material is available free of charge via the Internet at <http://pubs.acs.org>.

## REFERENCES

- Jensen, K. F., and Bjornberg, O. (1998) Evolutionary and functional families of dihydroorotate dehydrogenases. *Paths Pyrimidines* 6, 20–28.
- Baldwin, J., Farajallah, A. M., Malmquist, N. A., Rathod, P. K., and Phillips, M. A. (2002) Malarial dihydroorotate dehydrogenase. Substrate and inhibitor specificity. *J. Biol. Chem.* 277, 41827–41834.
- Gero, A. M., and O'Sullivan, W. J. (1985) Human spleen dihydroorotate dehydrogenase: properties and partial purification. *Biochem. Med.* 34, 70–82.
- Norager, S., Jensen, K. F., Bjornberg, O., and Larsen, S. (2002) *E. coli* dihydroorotate dehydrogenase reveals structural and functional distinctions between different classes of dihydroorotate dehydrogenases. *Structure* 10, 1211–1223.
- Liu, S., Neidhardt, E. A., Grossman, T. H., Ocain, T., and Clardy, J. (2000) Structures of human dihydroorotate dehydrogenase in complex with antiproliferative agents. *Structure* 8, 25–33.
- Marcinkeviciene, J., Rogers, M. J., Kopcho, L., Jiang, W., Wang, K., Murphy, D. J., Lippy, J., Link, S., Chung, T. D., Hobbs, F., Haque, T., Trainor, G. L., Slee, A., Stern, A. M., and Copeland, R. A. (2000) Selective inhibition of bacterial dihydroorotate dehydrogenases by thiazolidinediones. *Biochem. Pharmacol.* 60, 339–342.
- Copeland, R. A., Marcinkeviciene, J., Haque, T. S., Kopcho, L. M., Jiang, W., Wang, K., Ecret, L. D., Sizemore, C., Amsler, K. A., Foster, L., Tadesse, S., Combs, A. P., Stern, A. M., Trainor, G. L., Slee, A., Rogers, M. J., and Hobbs, F. (2000) *Helicobacter pylori*-selective antibacterials based on inhibition of pyrimidine biosynthesis. *J. Biol. Chem.* 275, 33373–33378.
- Baldwin, J., Michnoff, C. H., Malmquist, N. A., White, J., Roth, M. G., Rathod, P. K., and Phillips, M. A. (2005) High-throughput screening for potent and selective inhibitors of *Plasmodium falciparum* dihydroorotate dehydrogenase. *J. Biol. Chem.* 280, 21847–21853.
- Heikkilä, T., Ramsey, C., Davies, M., Galtier, C., Stead, A. M., Johnson, A. P., Fishwick, C. W., Boa, A. N., and McConkey, G. A. (2007) Design and synthesis of potent inhibitors of the malaria parasite dihydroorotate dehydrogenase. *J. Med. Chem.* 50, 186–191.
- Palfey, B. A., Bjornberg, O., and Jensen, K. F. (2001) Specific inhibition of a family 1A dihydroorotate dehydrogenase by benzoate pyrimidine analogues. *J. Med. Chem.* 44, 2861–2864.
- Wolfe, A. E., Thymark, M., Gattis, S. G., Fagan, R. L., Hu, Y. C., Johansson, E., Arent, S., Larsen, S., and Palfey, B. A. (2007) Interaction of benzoate pyrimidine analogues with class 1A dihydroorotate dehydrogenase from *Lactococcus lactis*. *Biochemistry* 46, 5741–5753.
- Gao, G., Nara, T., Nakajima-Shimada, J., and Aoki, T. (1999) Novel organization and sequences of five genes encoding all six enzymes for *de novo* pyrimidine biosynthesis in *Trypanosoma cruzi*. *J. Mol. Biol.* 285, 149–161.
- Nara, T., Hshimoto, T., and Aoki, T. (2000) Evolutionary implications of the mosaic pyrimidine-biosynthetic pathway in eukaryotes. *Gene* 257, 209–222.
- Takashima, E., Inaoka, D. K., Osanai, A., Nara, T., Odaka, M., Aoki, T., Inaka, K., Harada, S., and Kita, K. (2002) Characterization of the dihydroorotate dehydrogenase as a soluble fumarate reductase in *Trypanosoma cruzi*. *Mol. Biochem. Parasitol.* 122, 189–200.
- Annoura, T., Nara, T., Makiuchi, T., Hashimoto, T., and Aoki, T. (2005) The origin of dihydroorotate dehydrogenase genes of kinetoplastids, with special reference to their biological significance and adaptation to anaerobic, parasitic conditions. *J. Mol. Evol.* 60, 113–127.
- Arakaki, T. L., Buckner, F. S., Gillespie, J. R., Malmquist, N. A., Phillips, M. A., Kalyuzhnyi, O., Luft, J. R., Detitta, G. T., Verlinde, C. L., Van Voorhis, W. C., Hol, W. G., and Merritt, E. A. (2008) Characterization of *Trypanosoma brucei* dihydroorotate dehydrogenase as a possible drug target: structural, kinetic and RNAi studies. *Mol. Microbiol.* 68, 37–50.
- Rowland, P., Nielsen, F. S., Jensen, K. F., and Larsen, S. (1997) The crystal structure of the flavin containing enzyme dihydroorotate dehydrogenase A from *Lactococcus lactis*. *Structure* 5, 239–252.
- Rowland, P., Norager, S., Jensen, K. F., and Larsen, S. (2000) Structure of dihydroorotate dehydrogenase B: electron transfer between two flavin groups bridged by an iron-sulphur cluster. *Structure* 8, 1227–1238.
- Hurt, D. E., Widom, J., and Clardy, J. (2006) Structure of *Plasmodium falciparum* dihydroorotate dehydrogenase with a bound inhibitor. *Acta Crystallogr., Sect. D: Biol. Crystallogr.* 62, 312–323.
- Hansen, M., Le Nours, J., Johansson, E., Antal, T., Ullrich, A., Löffler, M., and Larsen, S. (2004) Inhibitor binding in a class 2 dihydroorotate dehydrogenase causes variations in the membrane-associated N-terminal domain. *Protein Sci.* 13, 1031–1042.
- Bjornberg, O., Jordan, D. B., Palfey, B. A., and Jensen, K. F. (2001) Dihydrooxonate is a substrate of dihydroorotate dehydrogenase (DHOD) providing evidence for involvement of cysteine and serine residues in base catalysis. *Arch. Biochem. Biophys.* 391, 286–294.
- Bjornberg, O., Rowland, P., Larsen, S., and Jensen, K. F. (1997) Active site of dihydroorotate dehydrogenase A from *Lactococcus lactis* investigated by chemical modification and mutagenesis. *Biochemistry* 36, 16197–16205.
- Fagan, R. L., Jensen, K. F., Bjornberg, O., and Palfey, B. A. (2007) Mechanism of flavin reduction in the class 1A dihydroorotate dehydrogenase from *Lactococcus lactis*. *Biochemistry* 46, 4028–4036.
- Fagan, R. L., Nelson, M. N., Pagano, P. M., and Palfey, B. A. (2006) Mechanism of flavin reduction in class 2 dihydroorotate dehydrogenases. *Biochemistry* 45, 14926–14932.
- Jiang, W., Locke, G., Harpel, M. R., Copeland, R. A., and Marcinkeviciene, J. (2000) Role of lys100 in human dihydroorotate dehydrogenase: mutagenesis studies and chemical rescue by external amines. *Biochemistry* 39, 7990–7997.
- Jordan, D. B., Bisaha, J. J., and Piccollelli, M. A. (2000) Catalytic properties of dihydroorotate dehydrogenase from *Saccharomyces cerevisiae*: studies on pH, alternate substrates, and inhibitors. *Arch. Biochem. Biophys.* 378, 84–92.
- Marcinkeviciene, J., Jiang, W., Locke, G., Kopcho, L. M., Rogers, M. J., and Copeland, R. A. (2000) A second dihydroorotate dehydrogenase (Type A) of the human pathogen *Enterococcus faecalis*: expression, purification, and steady-state kinetic mechanism. *Arch. Biochem. Biophys.* 377, 178–186.
- Norager, S., Arent, S., Bjornberg, O., Ottosen, M., Lo Leggio, L., Jensen, K. F., and Larsen, S. (2003) *Lactococcus lactis* dihydroorotate dehydrogenase A mutants reveal important facets of the enzymatic function. *J. Biol. Chem.* 278, 28812–28822.
- Rowland, P., Bjornberg, O., Nielsen, F. S., Jensen, K. F., and Larsen, S. (1998) The crystal structure of *Lactococcus lactis* dihydroorotate dehydrogenase A complexed with the enzyme reaction product throws light on its enzymatic function. *Protein Sci.* 7, 1269–1279.
- Mohsen, A. W., Rigby, S. E., Jensen, K. F., Munro, A. W., and Scrutton, N. S. (2004) Thermodynamic basis of electron transfer in dihydroorotate dehydrogenase B from *Lactococcus lactis*: analysis by potentiometry, EPR spectroscopy, and ENDOR spectroscopy. *Biochemistry* 43, 6498–6510.
- Inaoka, D. K., Takashima, E., Osanai, A., Shimizu, H., Nara, T., Aoki, T., Harada, S., and Kita, K. (2005) Expression, purification and crystallization of *Trypanosoma cruzi* dihydroorotate dehydrogenase complexed with orotate. *Acta Crystallogr., Sect. F: Struct. Biol. Cryst. Commun.* 61, 875–878.
- Hartree, E. F. (1972) Determination of protein: a modification of the Lowry method that gives a linear photometric response. *Anal. Biochem.* 48, 422–427.
- Otwinowski, Z., and Minor, W. (1997) Processing of X-ray diffraction data collected in oscillation mode. *Methods Enzymol.* 276, 307–326.
- Vagin, A., and Teplyakov, A. (1997) MOLREP: an automated program for molecular replacement. *J. Appl. Crystallogr.* 30, 1022–1025.
- Sariego, I., Annoura, T., Nara, T., Hashimoto, M., Tsubouchi, A., Iizumi, K., Makiuchi, T., Murata, E., Kita, K., and Aoki, T. (2006) Genetic diversity and kinetic properties of *Trypanosoma cruzi* dihydroorotate dehydrogenase isoforms. *Parasitol. Int.* 55, 11–16.



36. Guex, N., and Peitsch, M. C. (1997) SWISS-MODEL and the Swiss-PdbViewer: an environment for comparative protein modeling. *Electrophoresis* 18, 2714–2723.
37. Brunger, A. T., Adams, P. D., Clore, G. M., DeLano, W. L., Gros, P., Grosse-Kunstleve, R. W., Jiang, J. S., Kuszewski, J., Nilges, M., Pannu, N. S., Read, R. J., Rice, L. M., Simonson, T., and Warren, G. L. (1998) Crystallography & NMR system: A new software suite for macromolecular structure determination. *Acta Crystallogr., Sect. D: Biol. Crystallogr.* 54, 905–921.
38. Emsley, P., and Cowtan, K. (2004) Coot: model-building tools for molecular graphics. *Acta Crystallogr. Sect. D: Biol. Crystallogr.* 60, 2126–2132.
39. Murshudov, G. N., Vagin, A. A., and Dodson, E. J. (1997) Refinement of macromolecular structures by the maximum-likelihood method. *Acta Crystallogr., Sect. D: Biol. Crystallogr.* 53, 240–255.
40. Ramachandran, G. N., and Sasisekharan, V. (1968) Conformation of polypeptides and proteins. *Adv. Protein Chem.* 23, 283–438.
41. Laskowski, R. A., MacArthur, M. W., Moss, D. S., and Thornton, J. M. (1993) PROCHECK: a program to check the stereochemical quality of protein structures. *J. Appl. Crystallogr.* 26, 283–291.
42. Collaborative Computational Project, N. 1994, The CCP4 suite: programs for protein crystallography. *Acta Crystallogr., Sect. D: Biol. Crystallogr.* 760–763.
43. Pinheiro, M. P., Iulek, J., and Cristina Nonato, M. (2008) Crystal structure of *Trypanosoma cruzi* dihydroorotate dehydrogenase from Y strain. *Biochem. Biophys. Res. Commun.* 369, 812–817.
44. Bjornberg, O., Gruner, A. C., Roepstorff, P., and Jensen, K. F. (1999) The activity of *Escherichia coli* dihydroorotate dehydrogenase is dependent on a conserved loop identified by sequence homology, mutagenesis, and limited proteolysis. *Biochemistry* 38, 2899–2908.
45. James, M. N., Sielecki, A. R., Brayer, G. D., Delbaere, L. T., and Bauer, C. A. (1980) Structures of product and inhibitor complexes of *Streptomyces griseus* protease A at 1.8 Å resolution. A model for serine protease catalysis. *J. Mol. Biol.* 144, 43–88.
46. Pauling, L. (1960) *The nature of the chemical bond*, 3rd ed., Cornell Univ. Press, Ithaca, NY.
47. Nielsen, F. S., Rowland, P., Larsen, S., and Jensen, K. F. (1996) Purification and characterization of dihydroorotate dehydrogenase A from *Lactococcus lactis*, crystallization and preliminary X-ray diffraction studies of the enzyme. *Protein Sci.* 5, 852–856.
48. Zheng, Y., and Ornstein, R. L. (1996) A theoretical study of the structures of flavin in different oxidation and protonation states. *J. Am. Chem. Soc.* 118, 9402–9408.
49. Leys, D., Tsapin, A. S., Nealsen, K. H., Meyer, T. E., Cusanovich, M. A., and Van Beeumen, J. J. (1999) Structure and mechanism of the flavocytochrome *c* fumarate reductase of *Shewanella putrefaciens* MR-1. *Nat. Struct. Biol.* 6, 1113–1117.
50. Rothery, E. L., Mowat, C. G., Miles, C. S., Walkinshaw, M. D., Reid, G. A., and Chapman, S. K. (2003) Histidine 61: an important heme ligand in the soluble fumarate reductase from *Shewanella frigidimarina*. *Biochemistry* 42, 13160–13169.
51. Madej, M. G., Nasiri, H. R., Hilgendorff, N. S., Schwalbe, H., and Lancaster, C. R. (2006) Evidence for transmembrane proton transfer in a dihaem-containing membrane protein complex. *EMBO J.* 25, 4963–4970.
52. Lancaster, C. R., Kroger, A., Auer, M., and Michel, H. (1999) Structure of fumarate reductase from *Wolinella succinogenes* at 2.2 Å resolution. *Nature* 402, 377–385.
53. Tao, X., Yang, Z., and Tong, L. (2003) Crystal structures of substrate complexes of malic enzyme and insights into the catalytic mechanism. *Structure* 11, 1141–1150.
54. Timm, D. E., Mueller, H. A., Bhanumoorthy, P., Harp, J. M., and Bunick, G. J. (1999) Crystal structure and mechanism of a carbon-carbon bond hydrolase. *Structure* 7, 1023–1033.
55. Hewitson, K. S., Lienard, B. M., McDonough, M. A., Clifton, I. J., Butler, D., Soares, A. S., Oldham, N. J., McNeill, L. A., and Schofield, C. J. (2007) Structural and mechanistic studies on the inhibition of the hypoxia-inducible transcription factor hydroxylases by tricarboxylic acid cycle intermediates. *J. Biol. Chem.* 282, 3293–3301.
56. Tsai, M., Koo, J., Yip, P., Colman, R. F., Segall, M. L., and Howell, P. L. (2007) Substrate and product complexes of *Escherichia coli* adenylosuccinate lyase provide new insights into the enzymatic mechanism. *J. Mol. Biol.* 370, 541–554.

B1800413R